The Astronomical Journal, 168:67 (24pp), 2024 August https://doi.org/10.3847/1538-3881/ad500a

Early Results from the HUMDRUM Survey: A Small, Earth-mass Planet Orbits TOI-1450A

Madison Brady[1], Jacob L. Bean[1], Andreas Seifahrt[2], David Kasper[1], Rafael Luque[1], Guðmundur Stefánsson[3,4,23], Julian Stürmer[5], David Charbonneau[6], Karen A. Collins[6], John P. Doty[7], Zahra Essack[8], Akihiko Fukui[9,10], Ferran Grau Horta[11], Christina Hedges[12], Coel Hellier[13], Jon M. Jenkins[14], Norio Narita[9,10,15], Samuel N. Quinn[6], Avi Shporer[16], Richard P. Schwarz[6], Sara Seager[16,17,18], Keivan G. Stassun[19,20], Stephanie Striegel[15,21], Cristilyn N. Watkins[6], Joshua N. Winn[3], and Roberto Zambelli[22]

[1] Department of Astronomy & Astrophysics, University of Chicago, Chicago, IL 60637, USA; mtbrady@uchicago.edu
[2] Gemini Observatory/NSF NOIRLab, 670 N. A'ohoku Place, Hilo, HI 96720, USA
[3] Department of Astrophysical Sciences, Princeton University, 4 Ivy Lane, Princeton, NJ 08540, USA
[4] Anton Pannekoek Institute for Astronomy, University of Amsterdam, Science Park 904, 1098 XH Amsterdam, The Netherlands
[5] Landessternwarte, Zentrum für Astronomie der Universität Heidelberg, Königstuhl 12, D-69117 Heidelberg, Germany
[6] Center for Astrophysics | Harvard & Smithsonian, 60 Garden Street, Cambridge, MA 02138, USA
[7] Noqsi Aerospace Ltd., 15 Blanchard Avenue, Billerica, MA 01821, USA
[8] Department of Physics and Astronomy, The University of New Mexico, 210 Yale Boulevard NE, Albuquerque, NM 87106, USA
[9] Komaba Institute for Science, The University of Tokyo, 3-8-1 Komaba, Meguro, Tokyo 153-8902, Japan
[10] Instituto de Astrofisica de Canarias (IAC), 38205 La Laguna, Tenerife, Spain
[11] Observatori de Ca l'Ou, Carrer de dalt 18, Sant Martí Sesgueioles 08282, Barcelona, Spain
[12] NASA Goddard Space Flight Center, 8800 Greenbelt Road, Greenbelt, MD 20771, USA
[13] Astrophysics Group, Keele University, Staffordshire, ST5 5BG, UK
[14] NASA Ames Research Center, Moffett Field, CA 94035, USA
[15] Astrobiology Center, 2-21-1 Osawa, Mitaka, Tokyo 181-8588, Japan
[16] Department of Physics and Kavli Institute for Astrophysics and Space Research, Massachusetts Institute of Technology, Cambridge, MA 02139, USA
[17] Department of Earth, Atmospheric and Planetary Sciences, Massachusetts Institute of Technology, Cambridge, MA 02139, USA
[18] Department of Aeronautics and Astronautics, Massachusetts Institute of Technology, 77 Massachusetts Avenue, Cambridge, MA 02139, USA
[19] Department of Physics and Astronomy, Vanderbilt University, Nashville, TN 37235, USA
[20] Department of Physics, Fisk University, Nashville, TN 37208, USA
[21] SETI Institute, Mountain View, CA 94043, USA
[22] Società Astronomica Lunae, Castelnuovo Magra, Italy
Received 2024 March 12; revised 2024 May 6; accepted 2024 May 15; published 2024 July 10

Abstract

M-dwarf stars provide us with an ideal opportunity to study nearby small planets. The HUnting for M Dwarf Rocky planets Using MAROON-X (HUMDRUM) survey uses the MAROON-X spectrograph, which is ideally suited to studying these stars, to measure precise masses of a volume-limited (<30 pc) sample of transiting M-dwarf planets. TOI-1450 is a nearby (22.5 pc) binary system containing a M3 dwarf with a roughly 3000 K companion. Its primary star, TOI-1450A, was identified by the Transiting Exoplanet Survey Satellite (TESS) to have a 2.04 days transit signal, and is included in the HUMDRUM sample. In this paper, we present MAROON-X radial velocities (RVs) which confirm the planetary nature of this signal and measure its mass at nearly 10% precision. The 2.04 days planet, TOI-1450A b, has $R_b = 1.13 \pm 0.04\,R_\oplus$ and $M_b = 1.26 \pm 0.13\,M_\oplus$. It is the second-lowest-mass transiting planet with a high-precision RV mass measurement. With this mass and radius, the planet's mean density is compatible with an Earth-like composition. Given its short orbital period and slightly sub-Earth density, it may be amenable to JWST follow-up to test whether the planet has retained an atmosphere despite extreme heating from the nearby star. We also discover a nontransiting planet in the system with a period of 5.07 days and a $M \sin i_c = 1.53 \pm 0.18\,M_\oplus$. We also find a 2.01 days signal present in the systems's TESS photometry that likely corresponds to the rotation period of TOI-1450A's binary companion, TOI-1450B. TOI-1450A, meanwhile, appears to have a rotation period of approximately 40 days, which is in line with our expectations for a mid-M dwarf.

Unified Astronomy Thesaurus concepts: M dwarf stars (982); Extrasolar rocky planets (511)

Materials only available in the online version of record: machine-readable table

1. Introduction

M dwarfs are ideal targets for the discovery of exoplanets, as many detection methods have signal amplitudes inversely proportional to the size of the host star. Atmospheric characterization surveys, using instruments like JWST, are similarly well suited to small stars. This fact, combined with the extreme abundance of M dwarfs in the Universe, means that we expect to find a large number of small, rocky planets around M dwarfs, and that the compositions, atmospheres, and formation histories of these planets should be relatively easy to study compared to similar planets around Sun-like stars.

Predictions of the single-transit detection capabilities of JWST found that the majority of rocky planets with detectable

[23] NASA Sagan Fellow.

atmospheric molecules orbit stars within 10 pc and with effective temperatures $T_{\rm eff} < 3400$ K (Wunderlich et al. 2019). This highlights the importance of precisely measuring the properties of M-dwarf planets in our solar neighborhood. While longer campaigns would allow us to target warmer and more distant stars, these targets would be far more resource intensive.

While it is relatively easy to study M-dwarf planets, they may differ substantially from planets around hotter stars. First, M dwarfs tend to have much longer active periods than other types of stars, and possess more frequent and more energetic flare activity during these periods (see, e.g., Hawley et al. 2000, for more details). These events could contribute to the vaporization of any surface oceans, resulting in substantial water loss as the water dissociates in the atmosphere and the hydrogen escapes to space (Luger & Barnes 2015). Vaporized oceans could contribute to a strong abiotic O_2 signature, which could be detected with JWST (Fauchez et al. 2020) and tell us whether or not a planet's surface is dessicated. However, these signatures may be difficult to detect, as the high stellar activity and flare rate of M dwarfs could contribute to rapid planet atmosphere escape compared to planets at equivalent instellations around more luminous stars (Tilley et al. 2019). As escape results in thinner atmospheres with higher mean molecular weights, M-dwarf planetary atmospheres may be difficult to characterize with instruments like JWST.

Additionally, due to the dramatic lowering of an M dwarf's luminosity as it moves onto the main sequence (Baraffe et al. 2015), planets' instellations change drastically over their lifetimes. An in situ planet around a M dwarf likely received a much larger amount of radiation in the past than it does today. As the relative location of the snow line during planet formation dictates what sorts of planetesimals are incorporated into a forming planet, this may mean that planets which are currently in the habitable zone (HZ) formed when the snow line was far away (Mulders et al. 2015). This would result in M-dwarf planets having volatile-poor compositions with higher densities than planets at similar instellations around other types of stars. This has important implications with respect to the expected yields of transiting atmosphere surveys, as well as the generalizability of their results.

This situation is further complicated by the sample of M-dwarf planets studied in Luque & Pallé (2022), who found that low-radius M-dwarf planets can largely be split into two populations, and interpreted those populations as rocky planets (like Earth) and planets that are 50% water by mass. It is unlikely for these water-rich planets to form so close to the host star, so these strange targets may be planets that formed beyond the ice line (where the rock-to-volatile ratio is about 1:1; see Marboeuf et al. 2014; Thiabaud et al. 2014) and migrated inwards toward their host star (which has been shown to be possible in the population synthesis models by Burn et al. 2021). However, Rogers et al. (2023) have shown that it is possible for a similar population partitioning to be caused by a divide between rocky cores and planets with massive hydrogen atmospheres, which is the more familiar explanation for the well-known exoplanet radius gap (Fulton et al. 2017). Understanding which of these scenarios is more likely could have a dramatic impact on our understanding of M-dwarf planet formation and habitability.

To evaluate these hypotheses, we need to measure the compositions of a large, relatively unbiased sample of M-dwarf planets. As planets of different compositions can have very similar masses and radii (see, e.g., the mass–radius models included in Zeng et al. 2019), it is vital to collect high-precision masses and radii for nearby M-dwarf planets with wide-field and/or ground-based instruments. This will allow us to properly prioritize targets for follow-up with expensive single-target instruments like JWST. Precise mass measurements will also be helpful for atmospheric retrievals with JWST, as Batalha et al. (2019) found that a 20% planetary mass precision is necessary to perform precise planetary atmospheric retrievals. With these mass measurements, we will be able to understand whether or not M-dwarf planets tend to differ systematically than planets around FGK stars.

While many nearby M dwarfs have transiting planets with 5% precision radii measured with wide-field photometric surveys like Kepler (Borucki et al. 2010) and the Transiting Exoplanet Survey Satellite (TESS; Ricker et al. 2015), there is no accompanying radial velocity (RV) survey that seeks to provide every single one of these planets with precise masses. Thus, we are conducting HUnting for M Dwarf Rocky planets Using MAROON-X (HUMDRUM), a volume-limited survey of nearby ($d < 30$ pc) M-dwarf ($T_{\rm eff} < 4000$ K) planets with transits identified via TESS with MAROON-X. By selecting targets that TESS has identified, the biases of TESS can be estimated (using simulations such as Sullivan et al. 2015 and Brady & Bean 2022, or with more advanced methods) to inform the biases of this survey. The completeness of this survey will be discussed in greater detail in following papers.

In this paper, we present RV measurements of one of the targets in the 30 pc sample, TOI-1450A, and confirm the planetary nature of its 2.04 days transit signal. We are also able to measure the ≈40 days rotation period of the primary star, as well as identify a 2 days signal in the TESS photometry that may be due to the rotation of TOI-1450B. The planet's short orbital period places it well within the conservative limits for tidal locking from Barnes (2017), meaning that the planet is likely tidally locked over billion-year timescales. As the primary star is relatively cool ($T_{\rm eff} \approx 3400$ K) and nearby, it is relatively easy to observe with JWST. Its planet is likely rocky and contributes to the growing sample of small nearby rocky planets that are prime targets for follow-up with JWST.

In Section 2, we describe the TOI-1450 system. In Section 3, we describe the observations and data used in this paper. We characterize the stars in Section 4 and the planets in Section 5. We discuss the fit system parameters in Section 6, and provide a summary of our conclusions in Section 7.

2. The TOI-1450 System

TOI-1450 is a multiple-star system, consisting of an A and B component separated by a projected 76 au on-sky (Mugrauer & Michel 2020). At a distance of 22.44 pc (Gaia Collaboration 2020), the target falls in the 30 pc HUMDRUM sample. As described by the TESS catalog (Stassun et al. 2019), TOI-1450A is a $R_\star = 0.474\,R_\odot$ M dwarf with an effective temperature $T_{\rm eff} = 3407 \pm 157$ K. TOI-1450B is described by Mugrauer & Michel (2020) as an M dwarf with a temperature of around 3000 K. Relations from Giovinazzi & Blake (2022) indicate that, based on its Gaia RP magnitude, TOI-1450B has a mass of around $M_* = 0.14 \pm 0.01\,M_\odot$. TOI-1450A and TOI-1450B are separated by 3.″4 and are thus easily resolved by MAROON-X (Seifahrt et al. 2018), but not by TESS. The two stars are close enough on-sky that TOI-1450B is not identified

Table 1
Properties of TOI-1450A, the Host Star

Property	Value	Reference
R.A.	19:07:24.83	Gaia Collaboration (2020)
decl.	+59:05:09.36	Gaia Collaboration (2020)
Spectral type	M3.0V	Lépine et al. (2013)
J mag	8.457	Cutri et al. (2003)
H mag	7.820	Cutri et al. (2003)
K mag	7.565	Cutri et al. (2003)
$M_{\star,\,K_s}$ ($M_\odot$)	0.471 ± 0.020	Stassun et al. (2019)
$R_{\star,\,K_s}$ ($R_\odot$)	0.474 ± 0.014	Stassun et al. (2019)
$L_\star$ ($L_\odot$)	0.0027 ± 0.007	Stassun et al. (2019)
$M_{\star,\mathrm{SED}}$ ($M_\odot$)	0.480 ± 0.024	This work
$R_{\star,\mathrm{SED}}$ ($R_\odot$)	0.483 ± 0.025	This work
Distance (pc)	22.443 ± 0.045	Gaia Collaboration (2020)
P_{rot} (days)	30–40	This work
T_{eff} (K)	3437 ± 86	This work
[Fe/H]	-0.12 ± 0.17	This work
log g	4.76 ± 0.04	This work

separately in the Two Micron All Sky Survey (2MASS) catalog (Cutri et al. 2003; Skrutskie et al. 2006), meaning that the observed *JHK* magnitudes of the system are likely influenced by blending. Thus, it is important to consider the influence of TOI-1450B when evaluating any photometric signals. The stellar parameters of TOI-1450A are provided in Table 1.

3. Observations

3.1. MAROON-X Radial Velocities

MAROON-X (Seifahrt et al. 2018, 2022) is a high-precision echelle spectrograph mounted on the 8.1 m telescope Gemini-North. It has a wavelength coverage in the visible and near-infrared encompassing 500–920 nm, selected due to the expected density of M-dwarf spectral lines in this regime. The instrument has two CCDs, one "blue" (500–670 nm) and the other "red" (650–920 nm), which are both exposed simultaneously whenever a target is observed. These two channels are treated as separate instruments for the purposes of data analysis, as they are in different wavelengths and thus capture different stellar signals. The data are reduced with a `Python3` pipeline developed using tools that were originally developed for the CRIRES instrument (Bean et al. 2010), and the RVs are calculated using a version of `serval` (Zechmeister et al. 2020) updated to work with MAROON-X data. RVs are found by stacking the individual spectra to form a coadded template, which is then compared to the individual observations using least-squares fitting to find the individual exposure RVs. Telluric lines from Earth's atmosphere are fully masked to prevent them from skewing our analysis. MAROON-X observations are calibrated with etalon spectra, which are observed simultaneously with the science targets. The etalon spectra correct for velocity drifts of the spectrograph but are themselves prone to long-term drifts due to aging of the Zerodur spacer in the etalon optics. The long-term drifts as well as additional offsets between runs were calibrated out using the spectra of a Th-Ar lamp.

We observed TOI-1450A as a part of the HUMDRUM sample, observing the system 118 times between the months of 2021 April and 2023 July. As the planet has an orbital period very close to 2 days, we attempted to observe it multiple times a night to improve our phase coverage. The data are shown in Figure 1. Most exposures, observed simultaneously in the red and blue channels, were 10 minutes long, allowing for peak per-pixel signal-to-noise ratios (SNRs) of approximately 80 in the blue channel and 200 in the red channel. The higher signal in the red channel is expected due to the cool nature of the star. These peak SNRs translate to a per-measurement observed RV error of roughly 1.0 m s^{-1} in the blue channel and 0.6 m s^{-1} in the red.

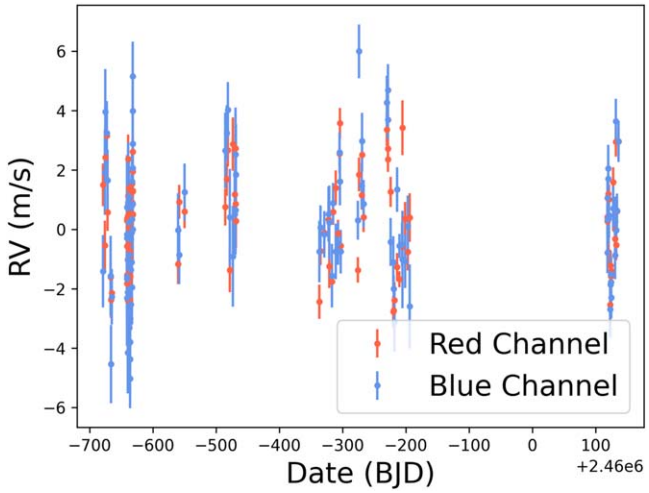

Figure 1. The MAROON-X RV observations of TOI-1450 with calibrated offsets between runs applied when available (and mean subtractions otherwise). The red-channel data are plotted in red, while the blue-channel data are plotted in blue.

Over the course of our observations, MAROON-X was operated in campaign mode on Gemini-North, sharing a port with several other instruments. Thus, the target was observed over the course of eight runs, discrete periods in which the instrument was connected to the telescope. There are frequently small (on the order of a few meters per second or less) RV offsets between these runs. These offsets are the result of both a constant, linear drift in our etalon calibrations over time (due to the aging of the Th-Ar lamp) in addition to some smaller, random instrumental shifts that are on the order of 1–2 m s^{-1} and occur between each run, likely as the result of connecting and disconnecting the fiber optic feed of the instrument from the telescope. Major instrumental failures or interruptions, such as the major cooler system shutdown on the instrument between 2021 April and May, also imparted additional offsets. These offsets were calibrated by the examination of RV standard stars, such as HD 88230, GJ 908, HD 3651, and HD 32147, during each MAROON-X run. Offsets between each MAROON-X run were then calculated using the measured RVs of these stars. These offsets (listed in Table 9) typically had errors on the order of 0.5 m s^{-1}, which we included as priors when fitting the RV data. We also included the effects of an observed linear RV drift observed in all MAROON-X targets in 2021 August, calibrated using several standard stars. As there were only three observations in August, any error on this drift calibration is unlikely to meaningfully affect our results.

We also observed TOI-1450B with MAROON-X twice in 2022 July, in an effort to characterize the star. As TOI-1450B is much dimmer than TOI-1450A, we performed 30 minutes exposures when observing this target. The resulting spectra had per-pixel SNRs of around 20 in the blue channel and 70 in the

Table 2
The First Several MAROON-X RVs Collected on TOI-1450A

Time (BTJD)	Channel	RV ($m\,s^{-1}$)	RV Error
2321.07733	Red	−5.89	0.72
2321.07733	Blue	−8.48	1.22
2324.09946	Red	−7.93	0.83
2324.09946	Blue	−5.15	1.44
2324.99367	Red	−4.97	0.68
2324.99367	Blue	−3.1	1.44

Note. The times are in BTJD (BJD-2,457,000). The rest of the RVs, as well as the values of the activity indicators, are available online.

(This table is available in machine-readable form in the online article.)

red channel. These data are insufficient to make a full characterization of the star's orbit but give us some insight into its spectral characteristics.

Our RVs are included in Table 2.

3.2. TESS Photometry

The TESS (Ricker et al. 2015) is a wide-field all-sky photometric survey that observes large chunks of the sky in 27 days sectors.

The transiting signal around TOI-1450 was originally identified after the SPOC conducted a transit search of sector 14 with an adaptive, noise-compensating matched filter (Jenkins 2002; Jenkins et al. 2010, 2020) identifying a threshold-crossing event for which an initial limb-darkened transit model was fitted (Li et al. 2019) and a suite of diagnostic tests were conducted to help determine the planetary nature of the signal (Twicken et al. 2018). The transit signature was also detected in a search of Full Frame Image (FFI) data by the Quick Look Pipeline at MIT (Huang et al. 2020a, 2020b). The TESS Science Office reviewed the vetting information and issued an alert on 2019 November 14 (Guerrero et al. 2021). The signal was repeatedly recovered as additional observations were made and the transit signature passed all the diagnostic tests presented in the Data Validation reports. According to the difference image centroiding tests, the host star is located within $5\farcs95 \pm 3\farcs48$ of the source of the transit signal.

TOI-1450 has been observed in 27 sectors (14–17, 19–26, 40–41, 47, and 49–60), and the data encompass dates from 2019 July through 2023 January. This is substantially more data than is available for most other TESS targets, which typically have only a few sectors' worth of data available. The data are available at a 2 minutes cadence, much faster than the 30 minutes cadence FFIs. Starting in sector 40, as a part of the TESS extended mission, the data are available with a 20 s cadence, allowing for further refinements in our understanding of the transit shape. The data from sectors 49–54 overlap with MAROON-X observations. All image data were reduced and analyzed by the TESS Science Processing Operations Center at NASA Ames Research Center (Jenkins et al. 2016).

Given the large pixels of TESS (21″), we checked the target field to estimate how much the transit signal was diluted by light from other stars and to ensure that we targeted the correct star for follow-up. The presence of nearby bright stars can result in smaller planetary transits and thus an underestimate of the planet's radius.

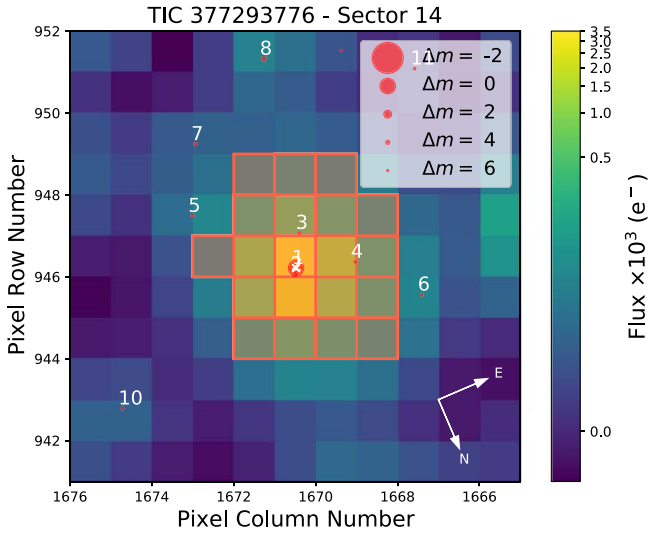

Figure 2. The crowding around TOI-1450. The sky, as seen by TESS in sector 14, is shown, with the specific aperture mask used marked in red. The star studied in this paper is marked with a white "×," while nearby stars (identified via Gaia) are shown as red circles, with their size representative of their G magnitude relative to TOI-1450A. Only stars with a $\Delta m_G \leqslant 6$ are shown, as the brightest stars contribute maximally to the light-curve flux contamination.

Investigating the crowding is fairly simple using the code `tpfplotter` (Aller et al. 2020), which plots the location of the TESS target, the TESS aperture mask, and the locations of any nearby stars found via the Gaia Early Data Release 3 (Gaia Collaboration 2020). Figure 2 shows the stars that have a chance of causing flux contamination in the sector 14 data. It is obvious that most of the stars that fall within the TOI-1450 aperture are substantially dimmer than TOI-1450A, with the brightest other star (TOI-1450B) having a $\Delta m_G = 3.78$.

We can determine the precise amount of dilution from the B star in the TESS light curve by estimating its T magnitude, m_T. Using the relationship between the Gaia colors and m_T from Stassun et al. (2019), we find that TOI-1450B has $m_T = 13.70$. This means that $\Delta m_T = 3.67$, corresponding to a dilution of around 3.3%. Even when also considering the other stars in the aperture, the dilution is less than 5%. If the transit is occurring around the B star, the dilution is >90%, meaning that the transit appears to be much shallower than it actually is. However, our MAROON-X RVs confirm that the 2 days transiting planet is orbiting around the primary star (see Section 5.2). Thus, the corrections we need to make to the light curve due to dilution are minimal, and are already performed by the Presearch Data Conditioning SAP (PDCSAP) algorithm (for more details on how crowding is dealt with by the PDCSAP algorithm, see Smith et al. 2012 and Stumpe et al. 2012, 2014).

3.3. ASAS Photometry

The TOI-1450 system has also been observed with ASAS-SN (Shappee et al. 2014; Kochanek et al. 2017), an all-sky photometric survey. The photometry, as of 2023 November 14, is shown in Figure 3. Given ASAS-SN's precise calibrations and long time baseline, it is a better photometer for examining long-term signals in the TOI-1450 light curve than TESS. However, as ASAS-SN images typically have cadences on the order of days (while the transits have 1 hr durations), they are not useful for detecting the planetary transits. ASAS-SN

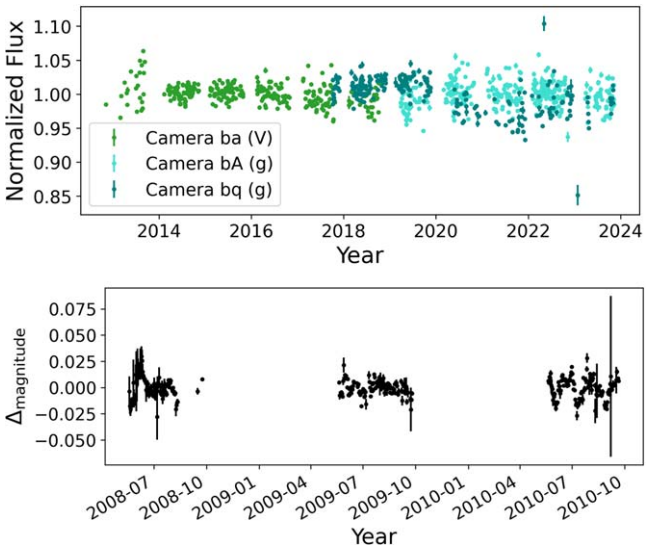

Figure 3. Top: ASAS-SN *V*- and *g*-band photometry of TOI-1450, normalized to unit mean flux. Bottom: 1 day binned WASP photometry of TOI-1450.

images have larger pixels (8″) than the separation between TOI-1450A and TOI-1450B, meaning that the observed light curves are the result of the blended light of the two targets. Given how much dimmer TOI-1450B is than TOI-1450A, however, we can expect TOI-1450A to be the dominant source of flux in the ASAS-SN curve.

TOI-1450 has flux measurements in *V* and *g* (filters centered on 551 and 480 nm, respectively) available in the ASAS-SN public database.[24] We downloaded flux measurements from the online database, processing them using the publicly available image-subtraction photometry pipeline, which performs photometry on coadded, image-subtracted data. As these light curves use coadded data, they contain fewer individual data points but are less noisy than the pure aperture photometry light curves. There were 309 total points in the *V* band and 572 total measurements in the *g* band.

The *V*-band data are older, encompassing times from 2012 November to 2018 October, with a median observation rate of once per every 3 days. The *g*-band data are the result of an overall instrument overhaul and are both more recent (2017 October to the present day) and have a more rapid cadence (with a median cadence of one observation every 2 days).

3.4. LCOGT Photometry

The TESS pixel scale is ∼21″ pixel^{-1} and photometric apertures typically extend out to roughly 1′, generally causing multiple stars to blend in the TESS photometric aperture. To attempt to determine the true source of the TESS detection, we acquired ground-based time-series follow-up photometry of the field around TOI-1450A as part of the TESS Follow-up Observing Program (Collins 2019).[25]

We observed two full transit windows of TOI-1450.01 on UTC 2022 July 6 and UTC 2022 August 17 in Pan-STARRS *z*-short band from the the Las Cumbres Observatory Global Telescope (LCOGT; Brown et al. 2013) 1 m network nodes at Teide Observatory on the island of Tenerife and McDonald Observatory near Fort Davis, Texas, United States, respectively. We also observed one full transit window on UTC 2022 September 3 simultaneously in Sloan g', r', and i', and Pan-STARRS *z*-short from the LCOGT 2 m Faulkes Telescope North at Haleakala Observatory on Maui, Hawai'i. The Faulkes Telescope North is equipped with the MuSCAT3 multiband imager (Narita et al. 2020). The images were calibrated by the standard LCOGT `BANZAI` pipeline (McCully et al. 2018) and differential photometric data were extracted using `AstroImageJ` (Collins et al. 2017). We used circular photometric apertures centered on TOI-1450A with radius 5.″8 for the 1 m observations and 4.″9 for the MuSCAT3 observation to extract the on-target differential photometry. The nearest known neighbor in the Gaia Data Release 3 (DR3) catalog (Gaia DR3 2155540255030594688; TOI-1450B) is ∼3.″3 north of TOI-1450A and is blended in the apertures. The light curves are included in the joint modeling described in Section 5.3. Using smaller ∼3″ photometric apertures, we tentatively detected the ∼0.5 ppt transit in TOI-1450A, but with higher scatter and systematics in the light curves. We also ruled out nearby eclipsing binaries within 2.′5 of TOI-1450A, except for the ∼3.″2 neighbor TOI-1450B, which is heavily contaminated by the ∼30 times brighter target star.

3.5. WASP Photometry

TOI-1450 was also observed by the Wide Angle Search for Planets (WASP) project at the Observatorio del Roque de los Muchachos (Pollacco et al. 2006) between the years of 2008 and 2010. The photometry is shown in Figure 3. The WASP transit search operated arrays of eight cameras using 200 mm, $f/1.8$ lenses with a broadband filter spanning 400–700 nm, backed by 2048 × 2048 CCDs giving a plate scale of 13.″7 pixel^{-1} (Pollacco et al. 2006). The large pixel size means that the WASP data also features blending between TOI-1450A and TOI-1450B on a single pixel. TOI-1450 was observed over spans of ∼120 days in each year. Observations on every clear night, with a typical 15 minutes cadence, accumulated 27,600 photometric data points.

4. Analysis

4.1. Stellar Parameter Fits

4.1.1. Direct Comparison to PHOENIX Spectra

As we currently lack an interferometic measurement of the star's radius, the parameters of TOI-1450 are those from the TESS catalog (Stassun et al. 2019), which takes its parameters from Muirhead et al. (2018), which makes use of the relations from Mann et al. (2015) and Mann et al. (2019) to estimate the stellar characteristics.

We can provide an independent measurement of the stellar parameters by comparing the MAROON-X spectra directly to stellar atmospheric models, allowing us to find the $T_{\rm eff}$, $\log g$, and [Fe/H] of TOI-1450 directly. We thus produced a code, with a similar methodology as that from Passegger et al. (2018), which estimates the stellar parameters by comparing the gathered MAROON-X spectrum to a set of interpolated, broadened `PHOENIX` (Husser et al. 2013) models. We consider both rotational broadening and the derived instrument broadening, order by order, of MAROON-X, which can be inferred directly from the etalon calibration files.

Instead of fitting a model to the entire MAROON-X spectrum, we have decided to primarily focus on regions that

[24] https://asas-sn.osu.edu/
[25] https://tess.mit.edu/followup

Table 3
The Rest-frame Wavelengths of the Regions Considered in Our Spectral Analysis

Line	λ_{min}	λ_{max}
TiO	7055.0	7074.0
TiO	7085.0	7114.0
TiO, Ca I	7125.0	7170.0
Ti I	8414.3	8415.0
Ti I	8428.2	8429.5
Ti I	8436.8	8438.7
Ti I, Fe I	8470.2	8471.1
Fe I	8516.0	8517.0
Fe I, Ti I	8676.5	8678.2
Ti I	8684.5	8685.8
Mg I	8808.7	8809.7
Fe I	8826.0	8827.5

Note. Inspired by Passegger et al. (2018) and slightly modified to include only regions where the models do not show strong systematic deviations from the data.

have shown to be sensitive to the parameters of interest, inspired by those used by CARMENES (Passegger et al. 2018), which is an instrument with very similar wavelength coverage to MAROON-X. Avoiding a full spectral comparison both makes our algorithm run substantially faster and allows us to focus primarily on the regions that are known to be the most indicative and/or modeled accurately. We have removed wavelength regions that are not typically observed by MAROON-X and have avoided including regions where the model spectra typically are very poor fits to the observed data. Table 3 indicates the precise wavelengths of these regions, as well as the molecular lines these regions typically encompass. We note that we have removed the K I region from our analysis, as we found that the PHOENIX models were poor fits to this region in our models.

The PHOENIX models from Husser et al. (2013) have varying temperatures, surface gravities, metallicities, and α-element abundances. For the sake of our fits, we included models with $4 < \log g < 6$, $2300 < T_{\rm eff} < 5000$ K, and $-1.0 < [{\rm Fe/H}] < 1.0$. We allow the α abundances of the models to remain fixed at the solar values, as PHOENIX models with nonzero α values are not available for stars under 3500 K. These limits are guided both by the the types of stars in our sample (M dwarfs) and the actual PHOENIX models available for download. We have found that all of the stars in the HUMDRUM sample fall well within these limits (according to the TESS parameter estimates).

We also applied rotational and instrumental broadening to these models before performing any fits. We first used the rotational convolution kernel from Gray (2008), and then applied a kernel that represents the instrumental broadening of MAROON-X (estimated from the instrument's etalon calibrations). After this, we resampled the models according to the MAROON-X wavelengths using the SpectRes Python module (Carnall 2017). We allowed the rotation to vary between $0 < v \sin i < 5$ km s^{-1}.

After performing broadening on each of these model spectra, we used the scipy module LinearNDInterpolator to interpolate between the model spectra, with grid spacing $\Delta T_{\rm eff} = 100$ K, $\Delta \log g = 0.5$, $\Delta[{\rm Fe/H}] = 0.5$ dex, and $v \sin i = 0.5$ m s^{-1}. The grid spacings for the first three parameters are guided by the available PHOENIX models, while the grid spacing of the stellar rotational velocities was user-specified and selected to be fine enough to account for the somewhat nonlinear relationship between stellar rotation and line broadening but coarse enough to allow for a reasonable computation time.

We also fit an additional error term σ, added in quadrature to the observed spectral flux errors, in order to get a sense of the scale of the systematic differences between the models and the data. As we normalized both the data and models such that the flux continuum was at a value of 1, this error value is expected to be between 0 and 1. We then performed Markov Chain Monte Carlo (MCMC) fits of our hightest-SNR observed spectra to the interpolated model spectra using the emcee package, with free parameters of $T_{\rm eff}$, [Fe/H], $v \sin i$, and σ. Our interpolations are performed in their entirety before the MCMC run is initiated instead of having the broadening recalculated at every step for the sake of reducing computation time. We did not independently fit $\log g$ because, much like Passegger et al. (2018), we found that there existed strong degeneracies between the fit surface gravity and the other parameters. We thus avoided fitting the $\log g$ directly, and instead estimated $\log g$ at each MCMC step. To do so, we used the estimated metallicity and the K_s magnitude from the 2MASS survey (Cutri et al. 2003) to calculate the stellar radius using the relation from Mann et al. (2015) and the stellar mass using the relation from Mann et al. (2019). Mann et al. (2015) quotes a 2.7% error on the estimated radius, while Mann et al. (2019) quotes a roughly 3% error, which overall results in our $\log g$ estimates having an additional error on the order of $\delta \log g = 0.025$–0.030. This systematic error will be added in quadrature to the fit error when listing the $\log g$ value.

In general, we found typical σ values that were on the order of 10 to 100 hundred times larger than the spectral flux errors. This indicates that the deviations between the PHOENIX models and our data are dominated by systematic differences between the models and data and not merely data errors. The fit parameter errors of this method are likely an underestimate, as there are significant discrepancies with the underlying models.

Passegger et al. (2022) found that, even when analyzing similar spectra, different methods for stellar parameter determination can report differences in $2022_{\rm eff}$ on the order of $\geqslant$100 K and [Fe/H] on the order of $\approx$0.1–0.3. Thus, instead of calibrating our code by looking at the results of other stellar parametric determinations, we estimate the errors on our parameters by comparing them directly to data. To estimate the accuracy of our algorithm, we compared our code's results to the known temperatures of nearby M dwarfs who have had these parameters estimated directly using interferometry. We use these to check our algorithm's accuracy, as their parameters were determined in a manner independent of the PHOENIX models. Table 4 lists the stars we use as references, along with their radii and temperatures. Observations of M dwarfs in binary systems with well-characterized primary stars may be a useful way to more accurately calibrate this relationship.

Figure 4 compares the temperatures of our calibrators derived via interferometry with those derived using our method. For each calibrator, we utilized the highest-SNR MAROON-X spectrum that we had available. It is obvious that our code is less accurate at temperatures above 4200 K and at temperatures at or below around 3200 K. At these temperatures, the code's sensitivity to temperature drops and the estimated temperatures appear to approach a constant value.

Table 4
Stars Observed by MAROON-X with Direct Interferometric Radius and Temperature Measurements, as Well as the Temperature and Metallicity Estimates from Our Code

Name	Radius ($R_\odot$)	$T_{\rm eff}$ (K)	References	Fit $T_{\rm eff}$ (K)	Fit [Fe/H]
GJ 15A	0.387 ± 0.002	3563 ± 11	(a)	3566^{+13}_{-10}	$-0.36^{+0.04}_{-0.03}$
GJ 273	0.32 ± 0.005	3253 ± 39	(b)	3342^{+17}_{-20}	$-0.30^{+0.04}_{-0.03}$
GJ 380	0.642 ± 0.005	4081 ± 15	(a)	4021^{+17}_{-19}	$-0.23^{+0.03}_{-0.02}$
GJ 406	0.159 ± 0.006	2657 ± 20	(b)	3209^{+13}_{-19}	0.14 ± 0.04
GJ 411	0.387 ± 0.004	3547 ± 40	(a)	3519^{+20}_{-74}	$-0.35^{+0.04}_{-0.15}$
GJ 447	0.196 ± 0.01	3264 ± 24	(b)	3289^{+10}_{-11}	-0.25 ± 0.03
GJ 486	0.339 ± 0.015	3291 ± 75	(c)	3387^{+9}_{-19}	$-0.13^{+0.02}_{-0.03}$
GJ 699	0.185 ± 0.001	3221 ± 32	(a)	3250^{+9}_{-8}	$-0.48^{+0.03}_{-0.02}$
GJ 725A	0.356 ± 0.004	3407 ± 15	(a)	3341^{+9}_{-8}	$-0.49^{+0.02}_{-0.01}$
GJ 725B	0.323 ± 0.006	3104 ± 28	(a)	3304 ± 7	-0.46 ± 0.03
GJ 729	0.205 ± 0.006	3162 ± 30	(b)	3316^{+9}_{-30}	$-0.39^{+0.03}_{-0.04}$
GJ 820A	0.665 ± 0.005	4548 ± 64	(a)	4356^{+8}_{-11}	-0.42 ± 0.02
GJ 820B	0.61 ± 0.018	3954 ± 28	(a)	4028^{+6}_{-4}	-0.32 ± 0.01

Notes. We note that errors associated with our fit values are purely taking the fit errors into account, and do not consider systematics. They are thus likely systematics.
References. (a) Boyajian et al. (2012), (b) Rabus et al. (2019), (c) Caballero et al. (2022).

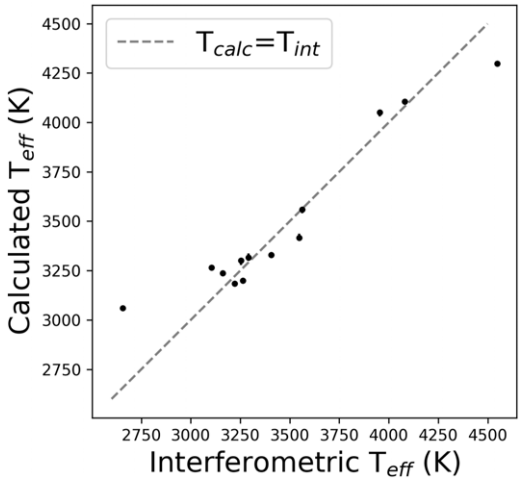

Figure 4. The interferometric temperatures of the calibrator stars compared to the MAROON-X estimations.

The lines we selected for analysis do not appear to be useful for measuring the properties of stars outside of this temperature range, which makes sense because our list was inspired by Passegger et al.'s (2018) studies of M dwarfs. While the code underestimates the temperatures for stars with temperatures above 4200 K, such stars are not included in the HUMDRUM sample and are thus not a problem. TOI-1450A (with an estimated temperature around 3400 K in the TESS catalog) is unlikely to fall outside of our range of sensitivity, but TOI-1450B, which is expected to have $T_{\rm eff} \approx 3000$ K, is likely too cool to obtain accurate results.

Overall, omitting Gl 406 and Gl 820A (both of which fall substantially outside of the sensitive temperature range) from our calibrator sample, we find a typical rms deviation between our fits and the interferometric temperatures of about $\sigma_T = 82$ K. This indicates the necessity of adding an additional error term in quadrature to the model-estimated $T_{\rm eff}$ (which is used to estimate $\log g$) on top of the statistical fit error and the systematic errors. As we are using similar spectral regions as Passegger et al. (2018), we quote a fit metallicity error of $\sigma_{\rm Fe/H} = 0.16$. Unfortunately, this number may not be accurate, but we do not have a sample of M dwarfs with independently verified metallicities to confirm our measurements.

With our code, we find that TOI-1450A has a $T_{\rm eff} = 3433 \pm 87$ K, $\log g = 4.76 \pm 0.04$, and [Fe/H] $= -0.12 \pm 0.17$. Its metallicity is similar to that of the Sun, and may be slightly subsolar, while its temperature is exactly what we would expect for a mid-M dwarf.

Unfortunately, TOI-1450B likely falls in the regime in which our temperature measurements are unreliable. An effort to measure its temperature yields $T_{\rm eff} = 3136 \pm 82$ K and its metallicity is measured as [Fe/H] $= 0.18 \pm 0.17$. Given the fact that the line list chosen seems to be unable to accurately estimate stellar parameters for stars with temperatures below about 3200 K, these values are likely inaccurate, though it is difficult to more precisely quantify these errors without more calibrator stars. We thus do not claim a measurement of the TOI-1450B stellar parameters.

4.1.2. SED Fitting

As an independent determination of the basic stellar parameters, we performed an analysis of the broadband spectral energy distribution (SED) of the star together with the Gaia DR3 parallax (with no systematic offset applied; see, e.g., Stassun & Torres 2021), in order to determine an empirical measurement of the stellar radius, following the procedures described in Stassun & Torres (2016) and Stassun et al. (2017, 2018). We pulled the the JHK_S magnitudes from 2MASS, the $W1$–$W4$ magnitudes from WISE, the z magnitude from PAN-STARRS, and the $GG_{\rm BP}G_{\rm RP}$ magnitudes from Gaia. We also utilized the absolute flux-calibrated spectrophotometry from Gaia. Together, the available data span the full stellar SED over the wavelength range 0.4–20 μm (see Figure 5).

We performed a fit using PHOENIX stellar atmosphere models (Husser et al. 2013), with the effective temperature ($T_{\rm eff}$) and metallicity ([Fe/H]) adopted from the analysis above. The extinction A_V was fixed at zero due to the close proximity of the system. The resulting fit (Figure 5) has a reduced χ^2 of 1.4. Integrating the model SED gives the bolometric flux at

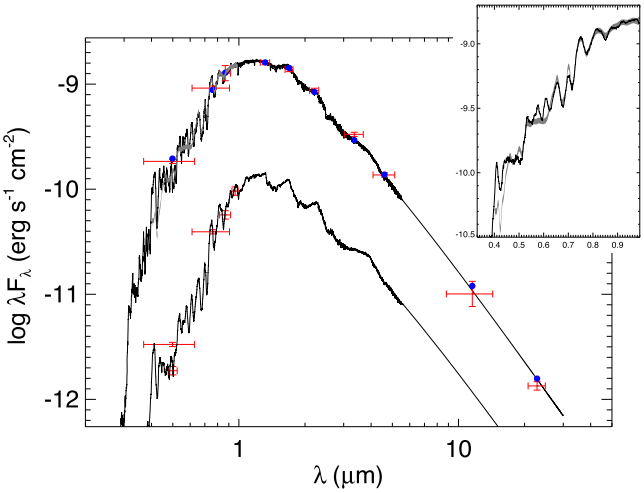

Figure 5. SED fit (upper black curve) to the observed photometry of TOI-1450A (red symbols). The absolute flux-calibrated Gaia spectrum is shown in gray and shown in detail in the inset plot. The SED of the faint companion star, TOI-1450B, is shown as the lower black curve atop its broadband photometric measurements (red symbols).

Earth, $F_{\rm bol} = 1.991 \pm 0.046 \times 10^{-9}$ erg s^{-1} cm^{-2}. Taking the $F_{\rm bol}$ and $T_{\rm eff}$ together with the Gaia parallax gives the stellar radius, $R_\star = 0.500 \pm 0.026\,R_\odot$. In addition, we can estimate the stellar mass from the empirical M_K relations of Mann et al. (2019), giving $M_\star = 0.496 \pm 0.025\,M_\odot$.

Next, we sought to account for the small flux contribution from TOI-1450B. To do this, we pulled the available broadband photometry from catalogs in which the companion is separately resolved, namely Gaia and PAN-STARRS. Next, we estimated the companion star's $T_{\rm eff}$ by interpolating the relative Gaia G magnitudes in the empirical tables provided in Pecaut & Mamajek (2013), and found that a PHOENIX model atmosphere of that $T_{\rm eff}$ (and adopting the same [Fe/H] as for TOI-1450A) indeed provides a good fit to the photometry (see Figure 5). Finally, we computed from this SED model the companion star's contribution to $F_{\rm bol}$ overall and to the K_S magnitude specifically, then recalculated the radius and mass for TOI-1450A, giving $R_\star = 0.483 \pm 0.025\,R_\odot$ and $M_\star = 0.480 \pm 0.024\,M_\odot$. These values agree quite closely with the values quoted by the TESS Input Catalog (TIC; STScI 2018; Stassun et al. 2019).

4.2. Stellar Rotation Period

4.2.1. TESS Photometry

The TESS photometry for this system is abundant, encompassing 27 sectors. We examined the TESS single-aperture photometry (SAP) for signs of stellar rotation, as long-term trends can sometimes be attenuated or removed by PDC when it identifies and removes instrumental effects. However, the SAP photometry may still contain meaningful instrumental systematics, so we will need to check to make sure our results are stellar in origin.

The 120 s cadence SAP photometric flux collected by TESS (and read in using `lightkurve`; Lightkurve Collaboration et al. 2018) is shown in Figure 6. Each sector has been mean-normalized to emphasize the variability and periodicity of the data as opposed to the slight photometric offsets between sectors. We examined the 120 s data (which have a longer time baseline than the 20 s data) for any evidence of rotational signals using the `PyAstronomy` (Czesla et al. 2019) implementation of the generalized Lomb–Scargle (GLS) periodogram (Zechmeister & Kürster 2009).[25] The resulting periodogram is shown in the middle panel of Figure 6.

The strongest peak in the GLS periodogram corresponds to a signal of around 40 days, which is visually obvious even when examining the raw data by eye (see the bottom panel of Figure 6). There is also a signal at around 27 days, which is likely merely related to the length of a TESS sector and is probably present due to systematics in the light curve. Finally, there is a third signal corresponding to 2.01 days, with a amplitude varying between 0.02% and 0.08%. This signal is very close to the observed planet transit period ($P = 2.04$ days), but appears to be distinct from the signal of the transiting planet, as it has a slightly different period (the 2.01 days peak in the periodogram is very narrow and does not encompass the transiting planet's period) and there is obvious sinusoidal variation on this timescale in the photometric data. Thus, this 2.01 days signal may be related to a star's rotation.

We thus notice two apparent rotation signals in the photometry, one at 40 days and one at 2.01 days. These could be representative of the rotation of the A and B stars, which are blended in the TESS pixel. While the primary is 30 times brighter than the secondary, the secondary is younger and thus may possess a proportionally stronger time-varying rotational signal. Thus, we cannot immediately determine which signal comes from which star based on the TESS data alone. In general, we would expect that a shorter-period signal belongs to the smaller star (see, e.g., the distributions of rotation periods with spectral type from Popinchalk et al. 2021). Taking the 97% dilution from the A star into account, if the 2 days signal does come from the B star, it actually corresponds to a 1%–3% amplitude signal in the TESS flux band. As a comparison, the rotation of TRAPPIST-1 (another late-M dwarf) manifests in its TESS photometry as a a roughly 0.6% signal. The slightly stronger amplitude of TOI-1450B may be the result of the star's shorter rotation period (and thus higher activity levels). Therefore, it would be logical for the 2 days signal to come from TOI-1450B, as its amplitude is reasonable compared to other short-period late-M dwarfs.

Additionally, a 40 days rotation signal would align with expectations from Popinchalk et al. (2021) for a field M3 star. However, the exact period of the 40 days rotation signal is somewhat uncertain, as TESS has problems with detecting signals with periods longer than the length of the 27 days TESS sector (Canto Martins et al. 2020). In Section 4.2.3, we study the Doppler broadening of the MAROON-X spectrum to resolve which rotation period is associated with which star, finding that the smaller star is likely the faster rotator, in agreement with theoretical expectations.

It is obvious that the system has flared multiple times during the TESS observation window, with one flare energetic enough to produce 15% of the combined system's luminosity. As lower-mass stars tend to flare more frequently (Davenport et al. 2019) and these two stars are likely the same age, the majority of these flares are likely the result of TOI-1450B and not the exoplanet host star. There is no clear photometric evidence that the star was flaring during any of our RV observations, so we were unable to confirm whether or not the flares come from TOI-1450A or TOI-1450B spectroscopically.

[26] https://github.com/sczesla/PyAstronomy

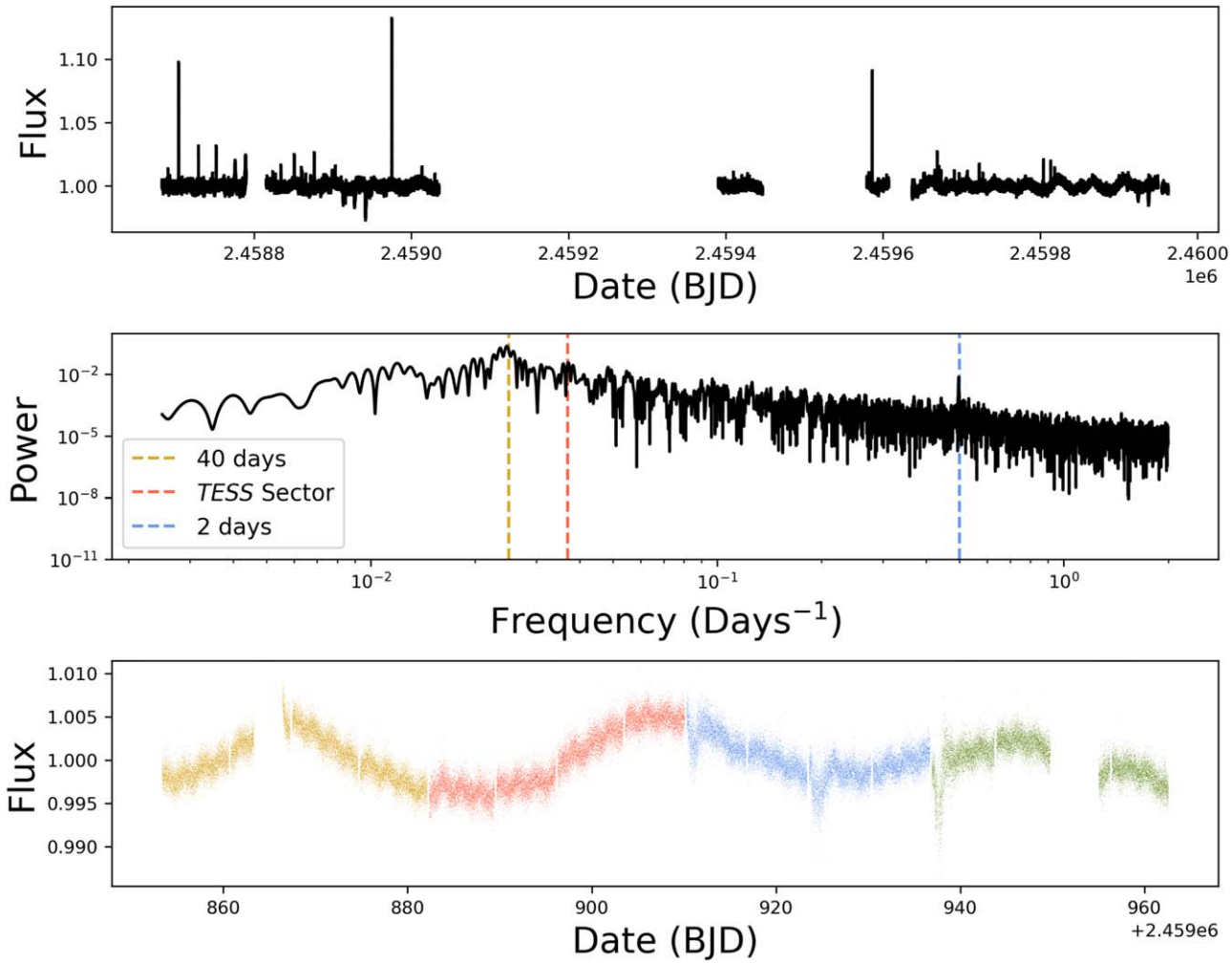

Figure 6. Top: the 120 s TESS SAP fluxes for the TOI-1450 system for sectors 14–60. Each sector's data is mean-normalized. Middle: GLS periodogram of the TESS 120 s data. Dashed vertical lines are drawn on the periodogram corresponding with the peaks at 40 days, 27 days (the length of a single TESS sector), and 2 days. Bottom: TESS photometry of sectors 57–60 the TOI-1450 system. The different sectors are colored differently in order to draw attention to where potential breaks in the baseline are expected. Sinusoidal variations on 40 days and 2 days timescales are obvious in these sectors.

4.2.2. ASAS-SN and WASP Photometry

We studied both the ASAS-SN and WASP photometry in order to gain further insight on the potential 40 days rotation period present in the TESS photometry. Both instruments had pixel sizes large enough to result in blending between TOI-1450A and TOI-1450B. The system appears stable, as the photometry, shown in Figure 3, shows no evidence of of long-term trends on year-length timescales. To search for signs of rotation, we produced GLS periodograms for each instrument, examining periods between 0.5 and 500 days. Overall, we expected both ASAS-SN and WASP to be more reliable than TESS over long periods of time.

Figure 7 shows the periodograms for three ASAS-SN cameras in two wavelength bands. In general, we typically expect to see stronger activity-induced variability in the bluer g band, and the g band also has more statistical power due to the larger number of observations. There are signals at around 1 and 172 days that likely correspond with the nightly observing cadence and half of 1 yr. Additionally, both the ba and bA cameras find a high false-alarm probability (FAP; >10%) signal at $P \approx 43$ days, but the signal is not present in the bq data. This signal coincides with the 40 days signal observed by TESS, strengthening the hypothesis that one of the stars in the

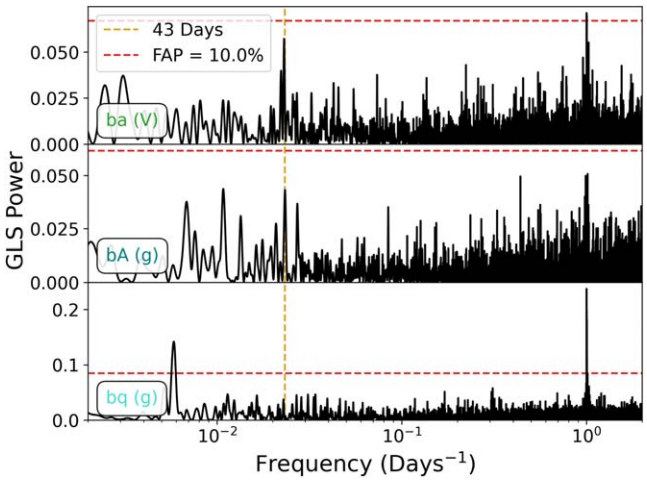

Figure 7. Lomb–Scargle periodograms of the ASAS-SN photometry. The red dashed horizontal line corresponds to a 1% false-alarm probability (FAP), and the golden vertical line indicates a 43 days period.

TOI-1450 system has a 40 days rotation period. The data are noticeably missing the strong 2.01 days signal noticed in the TESS photometry. However, this can be explained by the fact

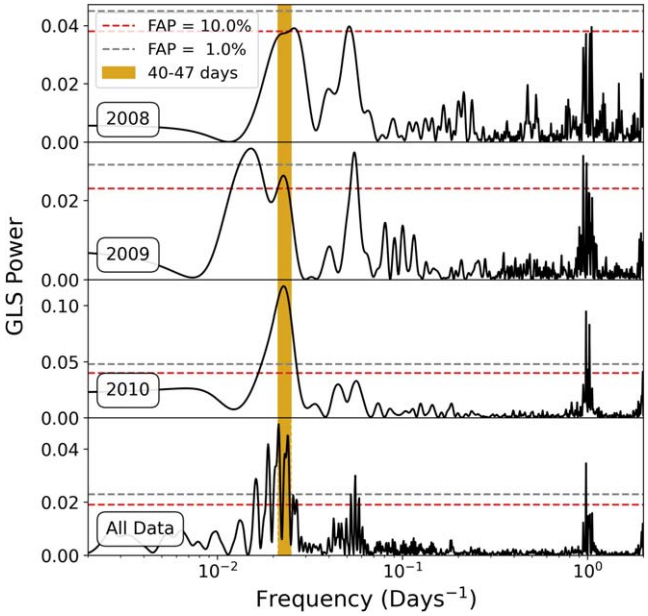

Figure 8. GLS periodograms of the WASP data. The red dashed horizontal line corresponds to a 1% false-alarm probability (FAP), and the golden vertical span indicates periods from 40 to 47 days. The signal at 1 day is likely related to the nightly sampling and is thus unlikely to be physical.

that the typical flux error for the ASAS-SN data (≈0.18%) is much larger than the amplitude of the rotational signal observed in the TESS data (≈0.03%).

Figure 8 shows the periodogram of the WASP photometry. Overall, we notice GLS periodogram peaks with a <1% FAP in between 40 and 47 days in all three data sets, but the 40 days peak is by far the strongest in the 2010 data. Both the 2008 and 2009 data sets feature stronger signals at 20 days, at half the proposed rotation period. The 2009 data feature a strong peak at around 60 days, but this signal is suspect given the fact that it is approximately half the length of the observing season. Overall, the data are consistent with the ≈40 days rotation period found by other instruments.

4.2.3. *Identifying the Fast Rotator by Estimating* v *sin* i

We can directly measure the projected rotational velocity $v \sin i$ of TOI-1450A and TOI-1450B by examining the line broadening present in the MAROON-X spectra. We can then check to see if this value is consistent with the observed 2 days periodicity in the TESS data. However, as MAROON-X has a resolution of roughly 85,000 (Seifahrt et al. 2018), this method will be imprecise for spectra with $v \sin i \lesssim 2\,\mathrm{km\,s^{-1}}$.

To estimate $v \sin i$, we used the cross-correlation (CCF) comparison method described in Gray (2005) and used with MAROON-X data in previous works (see Section 3.3 in Brady et al. 2023, for a more comprehensive description). With this method, we compared the spectra of TOI-1450A and TOI-1450B to other spectra taken by MAROON-X of known slow rotators with similar spectral types, which allowed us to estimate the rotational velocities of TOI-1450A and TOI-1450B.

As TOI-1450A is a M3 star, we compared it to Luyten's Star, a M3.5V star (Hawley et al. 1996) with a rotation period of 115.9 ± 19.4 days (Suárez Mascareño et al. 2015). Using this star as a template, we find that the $v \sin i$ of TOI-1450A is $1.8 \pm 0.6\,\mathrm{km\,s^{-1}}$, which is below the $v \sin i < 2\,\mathrm{km\,s^{-1}}$ lower limit of recordable rotational velocities given the MAROON-X resolution limits (see Brady et al. 2023, for more details). It is thus possible that the $v \sin i$ of TOI-1450A is below $2\,\mathrm{km\,s^{-1}}$, making the accuracy of this measurement suspect. Given the radius of TOI-1450A ($0.474\,R_\odot$), a 2 day rotation period would correspond to a measured rotational velocity of about $12\,\mathrm{km\,s^{-1}}$. This would easily be detectable by MAROON-X if the planet system had a low obliquity. The fact that the observed rotational velocity is below the measurement threshold of MAROON-X indicates that either the observed signal does not correspond to the rotational signal of TOI-1450A, or that the $\sin i$ of TOI-1450A is extremely low ($i < 10°$). The chances of the system randomly being oriented at such a low inclination is fairly small (<20%), but not impossible.

We also used this method to estimate the rotational velocity of TOI-1450B and compared it to the observed photometric signal. We used a spectrum of Teegarden's Star as a template, as it is the latest-type slow-rotating M dwarf observed by MAROON-X (with a rotation period of 99.6 ± 1.4 days Terrien et al. 2022). With it, we found that TOI-1450B has a rotation velocity of roughly $3.0 \pm 0.7\,\mathrm{km\,s^{-1}}$. Given TOI-1450B's mass of about $0.14\,M_\odot$, we would expect it to have a radius of around 0.15–$0.18\,R_\odot$ (comparing the mass to those of other late-M dwarfs, such as those in Parsons et al. 2018), which would correspond to an equatorial velocity of around 3.8–$4.5\,\mathrm{km\,s^{-1}}$ if it had a 2 day rotational period and we were observing it equator-on. We cannot eliminate the possibility that TOI-1450B has a rotation period of approximately 4 days and the observed 2 days signal in the photometry is due to persistent features on opposite hemispheres, though this possibility is slightly more discrepant with our measured rotation $v \sin i$. Thus, the observed signal could easily be explained by the rotation of TOI-1450B, especially if it is somewhat inclined relative to the transiting planet. Given its rapid rotation speed, it is unlikely to be the source of the 40 days rotation signal.

From this analysis, we conclude that the short-period rotation signal in the photometry is likely to come from TOI-1450B, which makes sense given the fact that it is much smaller than TOI-1450A and is thus likely to rotate more rapidly. This means that the 40 days signal is likely the product of TOI-1450A's rotation.

4.2.4. *Activity*

We can also estimate the rotation period of the star by studying the spectroscopic activity indicators. `serval` measures several activity indicators of the input spectra, including the chromatic index, differential line width, Hα index, the infrared Ca II triplet indices, and the Na I doublet indices. We can examine periodograms of these activity indicators to get a sense of the stellar rotation period. This examination is crucial to distinguishing genuine planetary signals from those that are merely stellar in nature, as we typically do not expect to see any planetary signals in the indicators.

The actual values of the activity indicators are shown in Figure 9. There are obvious offsets in the measured differential line widths (dLWs) between each MAROON-X run. This is a known issue and is believed to be due to small instrumental profile shifts as a result of the instrument front-end unit being unplugged from Gemini between each observation run. The fact that the offsets are not the same in the red and blue channels between 2021 April and May could explain the fact

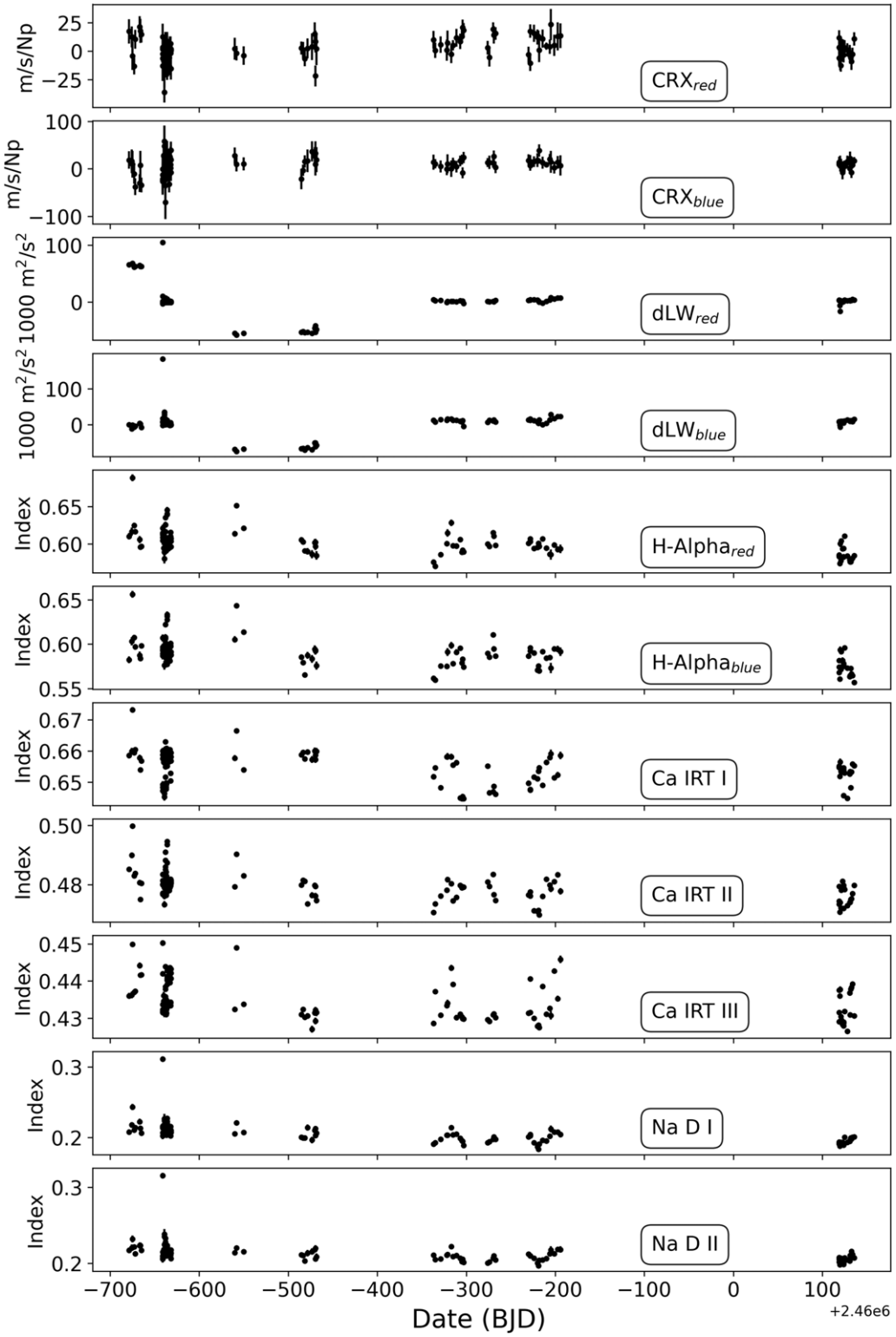

Figure 9. Time series of the MAROON-X activity indicators.

that our RV offsets between runs are chromatic at that time. There also appear to be long-period trends in the activity data that correspond to signals with $P = 1$ yr, which are likely related to the barycentric motion of the Earth causing telluric lines to influence our activity measurements.

There is an obvious outlier in the 2021 May blue-channel data in both the dLW measurements and in the Na D indices. A similar outlier of a smaller magnitude is also present in the red-channel dLW data at this time. However, there is no obvious outlier in the corresponding RV measurement. An examination of the spectrum in question reveals strong emission in the wings of the Na doublet at the time of observation. However, these emissive features are the result of sky emission of sodium and are masked out by `serval` when estimating RV. They are

also not included in serval's calculation of the actual Na D index, and thus cannot explain the observed large index shift. However, there are weaker telluric lines that cross the Na D line center during that exposure, and it is possible that they are responsible for the anomalous measurement. However, as the shift is also recorded in the measured chromatic index, it is possible that this observation was actually taken during some active event in which chromospheric Na D emission spiked. We also note a small outlier in the Hα index as recorded by both the red and blue channels in 2021 April, though an examination of the involved spectra does not show any obvious flare or telluric activity. As these observations may be the result of flares or failures by serval to accurately estimate the line indices, we removed them from our analysis for the purposes of creating the GLS periodograms.

The GLS periodograms of the activity indices are shown in Figure 10. In this figure, we removed the two observations that correlated with potential flare events, and also normalized the dLW data by subtracting the mean dLW value from each run. We see that most of the activity indicators used by serval have signals at the FAP $< 1\%$ level at around 40 days, with the exact periods varying between about 39–47 days. While these periods are longer than the length of a typical ($\approx$30 days) MAROON-X run, they are in agreement with the longer rotation period estimate from the TESS, ASAS-SN, and WASP data.

A closer examination of the lines studied showed that the centers of three of our known activity indicator lines (the redder Na doublet line and the bluest two Ca II lines) were contaminated by atmospheric tellurics during the majority of our observations, making their measured activity signals dubious. As measured trends in line indices between the two Na doublet lines agree despite the fact that one aligns with a known telluric region and the other does not, it appears that the telluric contamination in the line center is slight. This telluric contamination does appear to be more of an issue with regards to the Ca II lines, however, as the three data sets are less obviously correlated. To be conservative, if we ignore all activity indicators with known telluric crossings, we would only use the indices of Hα, the bluest Na doublet line, and the reddest Ca II line. All of these indicators have observed periodogram peaks around 39 days, however, so dropping the other lines from our analysis does not affect our results. It may be interesting in the future to attempt to fit out these lines (using a package like molecfit; see Kausch et al. 2015; Smette et al. 2015) for the purposes of determining telluric-corrected activity indicators, but is unnecessary in this case due to the relatively unambiguous nature of the signal in the other indices.

The activity indicators give us a clear sign that the rotation period of the A star is around 40 days. This supports our theory that TOI-1450A is not the 2.01 days rotator in the system, and that TOI-1450A has a rotation period of 40 days, which is in line with what is expected for a field M3 dwarf (Popinchalk et al. 2021).

If TOI-1450A has a rotation period of 40 days and TOI-1450B has a rotation period of 2 days, we can attempt to estimate the age of the system using gyrochronology. Using the relations from Engle & Guinan (2023) for old M2.5–6.5 dwarfs, we recovered an age of 3.4 ± 0.5 Gyr for TOI-1450A. However, this relationship does not account for temperature. We thus studied the gyrochrone of the 4 Gyr old M67 cluster from Dungee et al. (2022), and find that TOI-1450A is a slightly faster rotator than the 3400 K star observed in M67. This agreed with the sub-4 Gyr age estimate, indicating that TOI-1450A is a middle-aged star. Unfortunately, it is much more difficult to provide a gyrochronological estimate of TOI-1450B's age, as Pass et al. (2022) shows that there is significant variability in the spin-down rates of fully convective M dwarfs. While the 2 days rotation rate is not inconsistent with a $\approx$3 Gyr system age, acquiring a more precise system age from TOI-1450B is not possible. However, the rotation rates of the two stars are not inconsistent with each other, suggesting an overall system age of a few billion years.

5. Planet Fitting

5.1. Transit Photometry

We performed a fit to the transit photometry of the TOI-1450 system using juliet (Espinoza et al. 2019), which makes use of transit modeling from batman (Kreidberg 2015) and dynesty (Speagle 2020) to perform nested sampling. In our analysis of the TESS data, we considered the 2 minutes cadence data for light curves taken prior to the TESS extended mission, and the 20 s data for those taken afterwards (using the highest-cadence data available for each sector). We used the PDCSAP light curves in our analysis. For both the 120 and 20 s data, we performed 5σ clipping to reduce the influence of outliers on our analysis of the transits.

We searched the TESS data for planet signals using the transitleastsquares algorithm from Hippke & Heller (2019) to estimate the signal period and t_0. transitleastsquares searches for signs of planetary transits using a realistic model of transit ingress, egress, and stellar limb darkening. transitleastsquares found the 2.01 days rotation signal at a high confidence, but when the period search range is limited to exclude this signal it recovered the suspected planet at $P = 2.04392$ days and $t_0 = 2458685.34341$ BJD, which agrees with the values quoted online by the TESS team.

Before fitting the transits of the 2.04 days planet, we performed light-curve detrending. As discussed in Section 4.2.1, there are nonplanetary signals in the data due to stellar rotation. One of these signals, the rotation of TOI-1450B, has a period similar to the period of the suspected transiting planet. Due to the large amount of photometric data available for the TOI-1450 system, we did not simultaneously perform Gaussian process (GP) detrending and transit fitting of the data. Instead, we detrended the TESS data before fitting the transits. We detrended the data by fitting a GP (using an implementation of the approximate Matern kernel from celerite; Foreman-Mackey et al. 2017) to the 120 s PDCSAP TESS data from the system (the shorter-cadence 20 s data is unnecessary for studying a 2 days sinusoidal rotation signal), assuming an uninformative prior on the amplitude and a normal prior on the period centered around the suspected 2 days rotation period. We also masked out the transits (assuming the parameters from transitleastsquares) when fitting for the GP trend. The fit trend captured the 2 days variation signal in the photometry while preserving shorter-period variations (such as transits).

We then proceeded to fit the planet transits. First, we detrended the full TESS data set, including both 120 s data and 20 s data when it was available. To do this, we divided each TESS data point by the GP model. We did not perform the same extensive detrending for the ground-based transit data, as

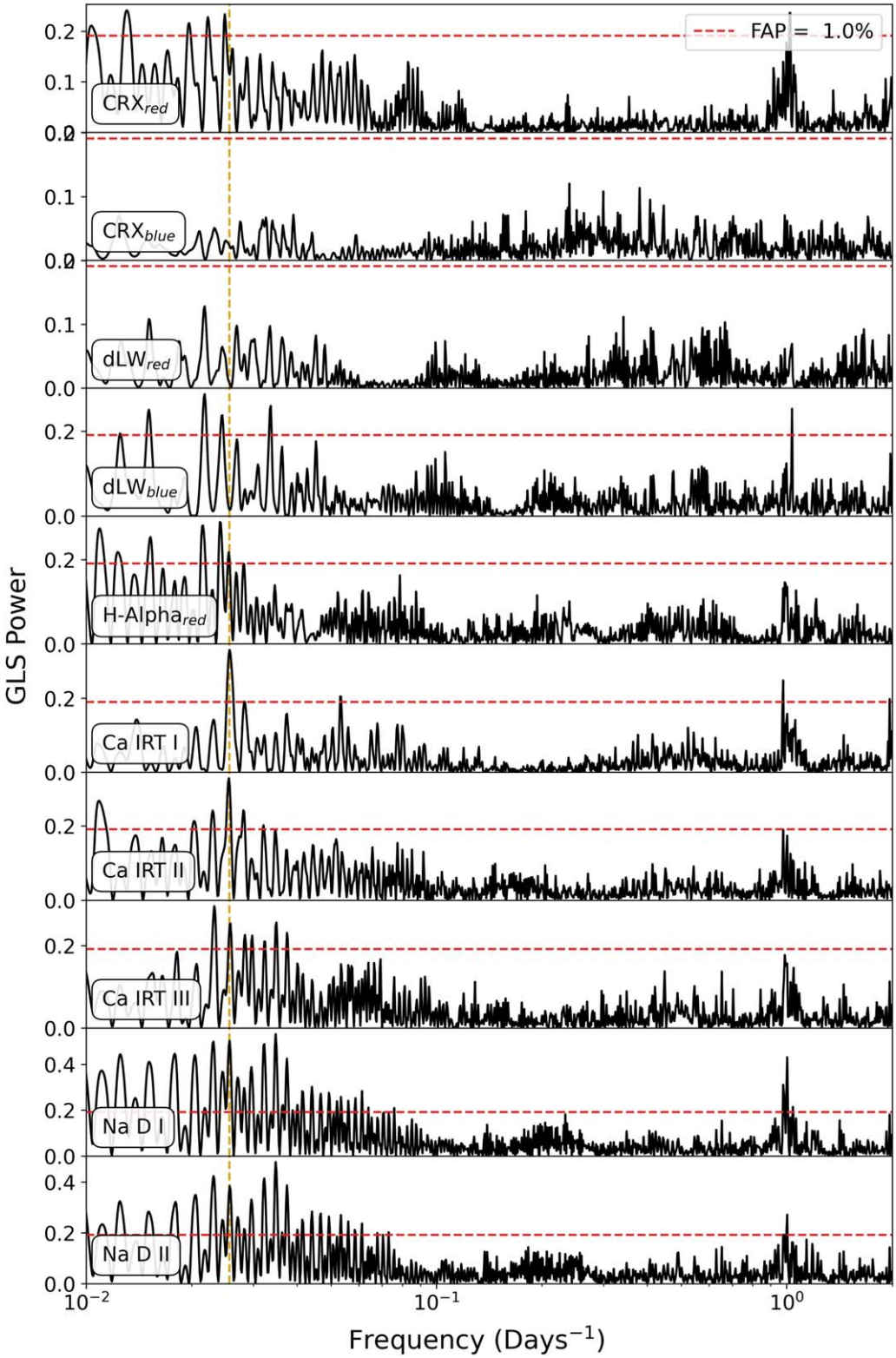

Figure 10. GLS periodograms of the signals present in the MAROON-X activity indicators, with outliers due to flares removed and the dLW data normalized to the mean within each run. The dashed gold line indicates the location of a 39 days period. A red dashed line corresponding to a false-alarm probability (FAP) of 1% is also shown.

we do not have enough data for the ground-based instruments to estimate the GP amplitude of each instrument. Once our detrending was complete, we identified TESS data points that were more than 45 minutes pre- or post-transit and omitted them from our transit analysis. This step was primarily performed as the extremely large amount of out-of-transit TESS data dramatically increased our computation time. A phase-folding analysis of the transit data suggested a transit

Table 5
The Priors Used in the Transit Fit as Well as the Resulting Fits

Fit Parameters	
P	N(2.04392, 0.0001)
t_0 (BJD)	N(2458685.34341, 0.005)
r_1	U(0, 1)
r_2	U(0, 1)
$\rho_\star$ (g cm^{-3})	N(6.23, 0.62)
μ	U(0, 1)
$\ln\sigma_{\rm ppm}$	U(ln(1), ln(10000))
q_1	U(0, 1)
q_2	U(0, 1)

Notes. The μ, $\ln\sigma$, q_1, and q_2 for the different instruments (the 120 s TESS data, the 20 s TESS data, the four separate LCO-MuSCAT3 colors, and the two separate LCO-Sinistro transit observations) are being fit separately, but all share the same priors so we omit listing them individually in this table.

Table 6
The Planet Parameters from the `juliet` Transit Fit to the Detrended TESS Data

Fit Parameters	
P (days)	2.0439276 ± 0.0000010
t_0 (BJD)	$2458685.34223 \pm 0.00042$
r_1	0.8256 ± 0.0143
r_2	0.0219 ± 0.0006
$\rho_\star$ (g cm^{-3})	6.32 ± 0.58
Derived Parameters	
$a/R_\star$	11.18 ± 0.35
R_p ($R_\oplus$)	1.130 ± 0.044
b	0.738 ± 0.022
I (degrees)	86.213 ± 0.227
$T_{\rm dur}$ (hr)	0.989 ± 0.013

duration of 70 minutes or less, so this masking was unlikely to remove any in-transit data.

We calculated the planet transit parameters using `juliet`, modeling the transit light curve of a planet with quadratic limb darkening. The priors used for the fit are listed in Table 5. We fit the period P and transit time t_0 using narrow priors informed by our `transitleastsquares` analysis, as the individual transits are very shallow and thus difficult to recover with uninformative priors.

We fixed the eccentricity at $e = 0$. This is because it is difficult to constrain the eccentricity from transit data alone unless a secondary transit is detected, transit timing variations (TTVs) are detected, or the stellar density is highly constrained (see, e.g., Van Eylen & Albrecht 2015). We will revisit the validity of this assumption when analyzing the RV data in later sections.

The priors for the limb-darkening coefficients, $R_p/R_\star$ ratio, and impact parameter b are set by the sampling methods used by `juliet`. To calculate the planet radius, we used the sampling technique described in Espinoza (2018), which parameterizes $R_p/R_\star$ and b using the uniformly distributed variables r_1 and r_2. The limb-darkening coefficients were sampled according to Kipping (2013) using the uniformly distributed variables q_1 and q_2. The stellar density $\rho_\star$ has priors based on the values for the mass and radius of TOI-1450A listed in Table 1. As TOI-1450A is a member of the TESS Cool Dwarf list, these values come from the observationally derived relations from Mann et al. (2015) and Mann et al. (2019), and are thus not likely to suffer from systematic modeling errors.

Our final analysis included the TESS data, the LCO-Sinistro data, and the LCO-MuSCAT3 data. We also fit parameters to the mean flux and jitter of each instrument to capture any variations between instrument flux baselines. We considered the 120 s data and 20 s data to be two separate data sets for the sake of fitting jitter, mean, and limb-darkening terms.

The resulting parameters for the transit fit are shown in Tables 6 and 7. The observed transit signal, in combination with the stellar radius from the TIC (Mann et al. 2015, using), is consistent with a $R_p = 1.13 \pm 0.04\ R_\oplus$ planet (similar in size to Earth) with an elevated impact parameter ($b = 0.74 \pm 0.02$). Our fits are primarily dependent upon the TESS data, as the ground-based data did not have enough statistical power to constrain the planet parameters. The transit data alone did not constrain the stellar density, with our fits merely recovering the prior. This is likely due to a combination of the short transit length and the shallow transit signal.

We also tested whether or not it was feasible to detect TTVs in the TOI-1450 data using `exoplanet` (Foreman-Mackey et al. 2020). We chose to use `exoplanet` (which uses MCMC sampling) instead of `juliet` (which uses nested sampling) at this step due to the large dimensionality of the problem. We first generated a light curve with `batman` with noise taken directly from the out-of-transit light curve from TESS for TOI-1450 and added 15 minutes TTVs, which are in line with some of the timing discrepancies observed by the ground-based observations. Overall, we found that we could not accurately recover a 15 minutes TTV signal from the simulated data, as the individual transits were too shallow compared to the noise to derive precise transit times. Thus, we did not attempt to perform a more complete TTV analysis of the TESS data for this system.

5.2. Radial Velocity

We fit the RV data for TOI-1450A using `juliet`. The framework is very similar to what we used in Section 5.1, but with different variables to account for the different observation methodologies. The fit planet parameters include K, the planetary RV semi-amplitude, the period P, the time of conjunction t_0, the eccentricity e, and the argument of periastron ω. We parameterized e and ω as $\sqrt{e}\cos\omega$ and $\sqrt{e}\sin\omega$, and allowed these values to vary between -1 and 1. The t_0 and P priors were taken from the transit fits in Table 6. We also included some additional fit parameters to reflect instrumental effects. As the red and blue channels cover different wavelength ranges, we allowed them to have separate fit mean and jitter terms. We have priors on the RV offsets between several of the individual MAROON-X data runs (described in Section 3.1; see Table 9 for the numerical values), so these priors were included on the fit means. There were several runs in which offset calibration was impossible due to insufficient or ambiguous calibration data. When no offset priors were available, we set broad uninformative priors on the individual offsets.

5.2.1. Model Selection

To properly characterize the transiting planet, we must determine if there are any additional planets in the system and their characteristics. We performed a simple period search of

Table 7
The Instrument Parameters from `juliet` Transit Fit to the Detrended TESS Data

Instrument	μ (ppm)	σ (ppm)	q_1	q_2	u_1	u_2
$TESS_{120\ s}$	-3 ± 23	6^{+17}_{-4}	$0.29^{+0.26}_{-0.18}$	$0.32^{+0.37}_{-0.23}$	0.32 ± 0.27	0.16 ± 0.31
$TESS_{20\ s}$	10 ± 18	865^{+25}_{-25}	$0.32^{+0.19}_{-0.14}$	$0.54^{+0.30}_{-0.34}$	0.57 ± 0.31	-0.04 ± 0.33
$Sinistro_{Jul}$	31 ± 96	1141^{+88}_{-83}	$0.57^{+0.29}_{-0.36}$	$0.51^{+0.33}_{-0.34}$	0.66 ± 0.48	-0.01 ± 0.42
$Sinistro_{Aug}$	6 ± 86	802^{+84}_{-83}	$0.54^{+0.31}_{-0.34}$	$0.53^{+0.32}_{-0.34}$	0.66 ± 0.47	-0.04 ± 0.41
$MuSCAT3_g$	-4 ± 61	569^{+73}_{-72}	$0.56^{+0.30}_{-0.34}$	$0.50^{+0.33}_{-0.32}$	0.64 ± 0.46	0.01 ± 0.41
$MuSCAT3_r$	39 ± 66	1718^{+56}_{-52}	$0.59^{+0.28}_{-0.34}$	$0.51^{+0.33}_{-0.34}$	0.67 ± 0.48	-0.01 ± 0.42
$MuSCAT3_i$	25 ± 71	2248^{+55}_{-56}	$0.44^{+0.36}_{-0.30}$	$0.44^{+0.35}_{-0.30}$	0.49 ± 0.42	0.06 ± 0.37
$MuSCAT3_z$	26 ± 56	2093^{+46}_{-45}	$0.45^{+0.34}_{-0.31}$	$0.45^{+0.36}_{-0.31}$	0.51 ± 0.42	0.05 ± 0.38

our RV data by progressively fitting circular Keplerian orbits to GLS periodogram peaks using `juliet`, searching for peaks between 0.5 and 50 days. Figure 11 shows some of these periodograms, as well as our window function. We ignored $P \approx 1$ day signals given the strong peak at that period in our window function.

First, we performed a simple zero-planet fit including the offset priors to get a sense of the signals present in the data. There was a peak at $P = 2.04$ days with a FAP $< 0.1\%$, corresponding to the period of the known transiting planet. The presence of this significant signal supports our statement that the transiting planet orbits this star and not TOI-1450B. While this peak was not the dominant one in the periodogram, we were certain of its period and phase from the transit data and thus fit it out first, using priors on P and t_0 from our analysis in Section 5.1.

After fitting out the transiting planet, the periodogram had several very-low-FAP (<0.1%) peaks remaining, one of which was at 20.2 days (likely corresponding to one half of the rotation period) and the other at 14.9 days. After attempting to fit it with a Keplerian, we found that the 14.9 days signal had a significantly higher amplitude in the blue channel of MAROON-X ($1.90 \pm 0.22\ m\ s^{-1}$) than it did in the red channel ($1.01 \pm 0.18\ m\ s^{-1}$). This indicates that it may be heavily influenced by either stellar activity or some kind of instrumental systematic. While it does not obviously have a timescale related to the stellar rotation period, it could potentially be an alias of the 20 days signal related to the 57 days peak in the window function (see the bottom panel of Figure 11). The 20 days signal is also chromatic ($1.64 \pm 0.18\ m\ s^{-1}$ in the blue channel and $0.95 \pm 0.21\ m\ s^{-1}$ in the red channel), supporting the hypothesis that it is related to stellar rotation. However, this analysis is complicated by the fact that most MAROON-X runs are 1–4 weeks long, making it hard to disentangle the influence of a long-period activity signal on any long-period planets. We thus hesitate to claim this signal as a planet despite its high significance.

As we are confident that the star has a rotation period of around 40 days, we next performed a fit including the transiting planet and a Keplerian at 20.2 days (as a Keplerian is an imperfect way to model an activity signal, we modeled it differently later on). After this fit, the significance of the 14.9 days signal was reduced and the highest residual peak was at 5.06 days. This 5.06 days signal may correspond to a second planet in the system. Fitting out the 5.06 days signal (using a uniform prior from 4 to 5.5 days) resulted in a forest of low-FAP peaks in the residual periodogram around 3.3 days. However, this final ≈3 days signal was difficult to fit, with its period strongly depending on our treatment of the rotation signal. It is possible that there is a planet around this period in the system (a planet at 3.18 or 3.39 days would be in a p, $q = 2$, 3 or p, $q = 1$, 2 three-body Laplace resonance with the other two planets, respectively), but the signal is currently too low to confirm its presence.

To understand the influence of aliasing on our inferred model, we performed an analysis of the TOI-1450A system using the ℓ_1 periodogram (Hara et al. 2017).[26] The ℓ_1 periodogram is similar to a Lomb–Scargle periodogram in that it searches for signals in unevenly sampled data, but is specifically designed to reduce the number of observed peaks due to aliasing. We performed a ℓ_1 periodogram analysis of all of the MAROON-X RV data, with the same offsets applied to the RVs as in Table 9 and mean subtractions when no calibrated offsets were available.

For the purposes of noise modeling, we considered a grid of models with different white noise ($\sigma_w = 0$–$1.5\ m\ s^{-1}$, $\Delta\sigma_w = 0.25\ m\ s^{-1}$), red noise ($\sigma_r = 0$–$1.5\ m\ s^{-1}$, $\Delta\sigma_r = 0.25\ m\ s^{-1}$), calibration noise ($\sigma_c = 0$–$1.5\ m\ s^{-1}$, $\Delta\sigma_c = 0.25\ m\ s^{-1}$), and red-noise timescales ($\tau = 1$, 2, 4, 10, 20, 40, 120 days). For each noise model, we computed the cross-validation score using the same methods as described in Hara et al. (2020). In general, for each noise model we selected signals with $\log_{10}\mathrm{FAP} < -0.5$. Then, the data were split into a randomly selected training and test set (with a 60/40 split). A sinusoidal model with the selected frequencies was fit on the training set, and the likelihood of this model was evaluated on the test set. This process was repeated 400 times for each noise model, and we quote the median of the likelihoods for each noise model as the cross-validation score.

Figure 12 shows the resulting FAPs and periods of the selected signals for the top 10 highest-ranking models (representative of about 0.5% of the models evaluated). We note the presence of both the transiting planet signal and the 5.06 days planet signal at FAPs that are less than 0.1%, indicating that these planets are present in the data. We also see signals at 15 and 20 days that correspond with the chromatic signals we have observed in our previous analysis which are unlikely to be planetary in origin. We also see a low-FAP signal at around 7.5 days, which corresponds with half of the 15 days signal and is thus also unlikely to be planetary in origin. Interestingly, we do see the presence of a signal at $P = 3.44$ days in this analysis, but the FAP is greater than 1% and thus we hesitate to claim it as a planet. More data may be necessary to confirm or deny the presence of this signal.

[27] https://github.com/nathanchara/l1periodogram

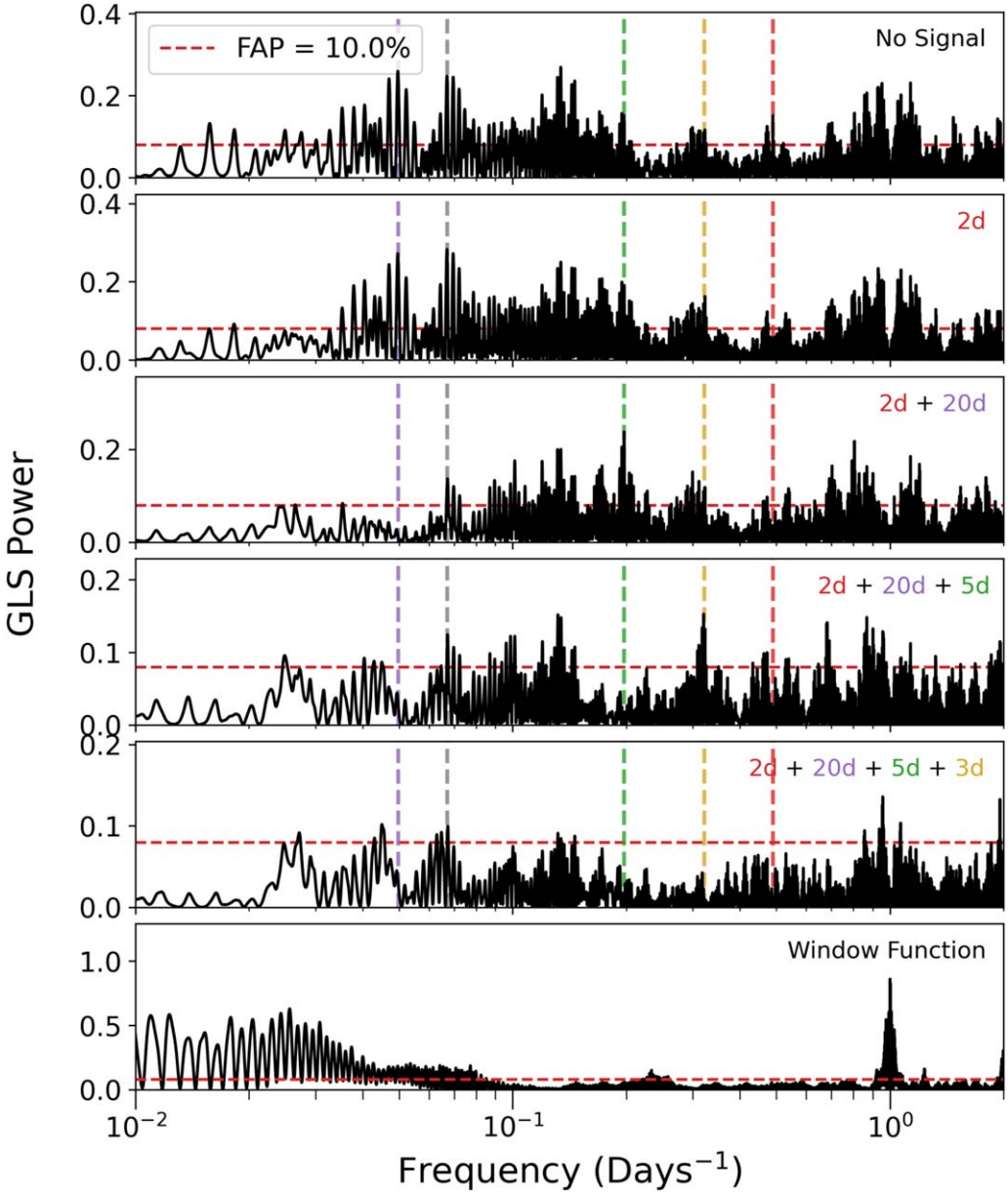

Figure 11. GLS periodograms of the RV data of TOI-1450 with various signals subtracted. Each panel has a note describing which signals have been subtracted from the data to produce the residual periodogram. The bottom panel shows the window function. A red dashed line corresponding to a FAP of 0.1% is shown on each plot. In addition, vertical dotted lines corresponding to the periods of the fit planets are also included. The red line is the 2.04 days signal, the gold is the ≈3 days signal, the green is the ≈5 days signal, the gray is the ≈15 days signal, and the purple is the 20 days signal.

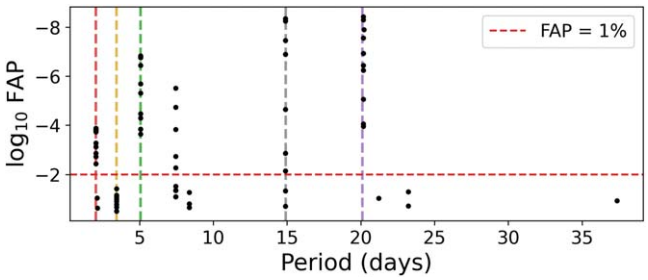

Figure 12. A ℓ_1 periodogram of the TOI-1450 RV data. Vertical dotted lines correspond to various periods. The red line is a 2.044 days signal, the gold a 3.44 days signal, the green a 5.06 days signal, the gray a 14.9 days signal, and the purple a 20.1 days signal. The horizontal dashed line corresponds to a 1% FAP.

Several other high-FAP signals were also identified in the ℓ_1 periodogram, but we do not claim planetary detections at these periods for similar reasons.

In summary, we identified the presence of signals corresponding to the known transiting planet ($P = 2.04$ days), as well as signals at approximately 5, 15, 20, and 3 days, though we suspect that the 15 days, 20 days, and 3 days signals may be related to stellar activity and/or systematics (or at least contaminated heavily by these effects). To investigate the significance of these signals, we performed nested sampling fits with normal priors centered around the identified periodogram peaks, and found the log evidence of each model with `juliet`.

We also included models in which we used GPs to model the stellar activity using a quasiperiodic kernel (see, e.g., Aigrain

et al. 2012; Stock et al. 2023). The quasiperiodic kernel is frequently used to model the effect of stellar activity on RVs and photometry, as it is able to reproduce the periodic signature of stellar rotation. The kernel is

$$\kappa(t - t') = \sigma_i^2 \exp\left(-\frac{\alpha(t - t')^2}{2} - \Gamma \sin^2\left(\frac{\pi(t - t')}{P_{\rm rot}}\right)\right), \quad (1)$$

where α is the inverse square of the correlation timescale (which usually corresponds with the spot evolution timescale), $P_{\rm rot}$ is the rotation period of the star, Γ describes the relative strength of the periodic to the aperiodic portion of the modeled signal, and σ is a wavelength-dependent parameter that describes the amplitude of the signal. The first term of the equation describes the aperiodic portion of the signal, and the second term describes the periodic portion. We fitted σ separately for the red and blue channels of MAROON-X but assumed all of the other GP parameters were instrument independent.

We set our GP priors by following the suggestions of Stock et al. (2023). We allowed $P_{\rm rot}$ to have a normal prior of 40 ± 3 days, which both encompasses the range of periods suggested by both the activity indicators and photometry. We set α such that the correlation timescale falls between 40 days and the length of our data collection, as it has been shown observationally that M dwarfs typically have spot evolution timescales longer than one rotation period (see, e.g., Robertson et al. 2020, and the references therein). We have allowed Γ to have a log-uniform prior from 0.01 to 10 following the suggestions of Stock et al. (2023), as very high values of Γ can result in GP overfitting. We have placed an upper limit of $4\,{\rm m\,s^{-1}}$ on σ, reflecting the degree of scatter observed in the RVs. The priors for our GPs are listed in Table 9 in Section 5.3.

The models examined, with their associated transiting planet masses and relative Bayesian evidences, are shown in Table 8. The model with the highest Bayesian evidence is the model that the data supports the most heavily, though we note that differences in ln$Z$ on the order of 1–2.5 only indicate weak-to-moderate evidence for a model, as discussed in Trotta (2008).

The four models with the highest evidence are a two-planet model featuring the transiting planet and the 5 days planet, as well as three three-planet models with the transiting planet, 5 days planet, and a 3 days, 15 days, or 20 days planet in addition. However, we are hesitant to select any of these three-planet models, as we have found in our previous analysis that the 15 days and 20 days signals in our data are highly chromatic and the 3 days signal has a broad period prior and cannot be recovered by the ℓ_1 periodogram with a $<1\%$ FAP. A closer look at our 3 days planet fit shows that the observed K of the 3 days planet is degenerate with the GP σ, meaning that the fit signal may be spurious and dependent upon how we chose to fit the stellar rotation. While it is possible that there is a 3 days planet in our data, we are hesitant to claim its presence given our data. If it does exist, it has a $K \leqslant 0.6\,{\rm m\,s^{-1}}$ and would thus likely need far more data to characterize accurately.

We also studied the influence of allowing the eccentricites of the planets to vary on our selected two-planet model. We found that, when allowing $\sqrt{e}\cos\omega$ and $\sqrt{e}\sin\omega$ to vary uniformly between -1 and 1 with our selected model, there was an increase in the evidence ($\Delta{\rm ln}Z = 7.1$), but the fit planet eccentricities were low (with broad posterior distributions) and the planet masses were consistent (within 0.3σ) with our circular-orbit model. We also found that allowing for nonzero eccentricities in our model without the fit GP resulted in essentially no change ($\Delta{\rm ln}Z = 0.8$). The fact that the planets only appear to have eccentric orbits with our GPs in place indicates that the small eccentricities observed may be the result of crosstalk between our Keplerian and stellar activity model and may not be physical. We thus conclude that we do not have sufficient evidence to conclude the planets have nonzero eccentricities. This aligns with the expectation that these short-period planets would likely have circular orbits, as the 2 days planet has a tidal circularization timescale of <2 Myr and the 5 days planet (assuming a rocky planet with a a nearly edge-on orbit and a larger radius than the 2 days planet) has a circularization timescale of <100 Myr. Given that this system is likely several billion years old, we expect the orbits to be near circular.

Thus, we select the two-planet model as our final model, as the models with higher evidences are likely the result of overly flexible GP fitting. We note that all of the models with higher evidence values have fit transiting planet masses within 1σ of our chosen model, so the transiting planet mass is not sensitive to our choice of model. Overall, the data support the presence of a transiting planet, as well as a planet with a 5.1 days period. There are longer-period signals present in the data, but it is difficult to disentangle aliases of potential rotational signals from long-period planets, as they seem to encompass similar ranges of periods. There also appears to be tentative evidence for a planet with a roughly 3 days period in the data (which could be in period commensurability with the two known planets), but we currently lack the statistical evidence to confirm it.

Table 8
List of All of the Models Used to Fit the Data with `juliet`, with the Associated Log Evidences and Mass of the Transiting Planet Signal

Model	$M_{\rm b}\sin i_{\rm b}$ ($M_\oplus$)	$d{\rm ln}Z$	$P_{\rm rot}$
⋯		−78.1	⋯
2d	1.24 ± 0.19	−60.3	⋯
2d, 5d	1.30 ± 0.16	−43.0	⋯
2d, 15d	1.18 ± 0.15	−27.8	⋯
2d, 20d	1.01 ± 0.19	−41.1	⋯
2d, 3d, 5d	1.29 ± 0.13	−40.6	⋯
2d, 5d, 15d	1.34 ± 0.09	−25.3	⋯
2d, 5d, 20d	1.16 ± 0.15	−16.4	⋯
2d, 3d, 5d, 15d	1.27 ± 0.09	−37.6	⋯
2d, 3d, 5d, 20d	1.25 ± 0.13	−11.5	⋯
2d, 3d, 5d, 15d, 20d	1.27 ± 0.16	−7.6	⋯
GP	⋯	−37.5	$39.9^{+1.7}_{-1.4}$
2d + GP	1.08 ± 0.13	−13.5	$38.0^{+1.4}_{-1.4}$
2d, 5d + GP	1.25 ± 0.13		$40.0^{+1.7}_{-1.4}$
2d, 15d + GP	1.05 ± 0.13	−13.5	$38.0^{+1.7}_{-1.6}$
2d, 20d + GP	1.15 ± 0.12	−7.0	$29.9^{+2.4}_{-1.4}$
2d, 3d, 5d + GP	1.26 ± 0.10	13.8	$38.9^{+0.5}_{-0.5}$
2d, 5d, 15d + GP	1.23 ± 0.12	8.5	$39.9^{+1.8}_{-1.5}$
2d, 5d, 20d + GP	1.24 ± 0.13	10.0	$39.5^{+1.9}_{-1.8}$

Notes. The log evidences are listed in terms of the difference between the final chosen model's evidence and the individual models' evidences, so lower numbers indicate more preferred models. The final chosen model is bolded. The typical error on ln$Z$ is 0.4–0.8, and is omitted from the table to save space.

5.3. Joint Transit and Radial Velocity Models

In this section, we perform a joint fit of the RV and transit data using `juliet` to determine our final planet parameters.

Before performing a joint fit to the RV and transit data, we checked the data with `transitleastsquares` to see if there were any transit signals consistent with the 5 days signal. A closer examination of the TESS light curves yields no obvious signals of a transiting planet at the newly identified planet's period and t_0. This is not surprising given the high impact parameter of TOI-1450A b. If TOI-1450A b and TOI-1450A c were coplanar, TOI-1450A c would have an impact parameter $b_c > 1$ and thus not transit.

As we do not find any evidence of any additional transiting planets in the TESS data, we used the RV data alone to characterize the nontransiting planet in the system. For the priors on the RV fit, we adopted the model from Section 5.2.1. This model included the transiting planet, a 5 days planet, and a quasiperiodic GP to model the ≈40 days rotational signal. The orbital eccentricities were fixed at zero. We use the same priors for the transit model that we used in Section 5.1, with the same data and detrending techniques. Our priors for the joint fit are listed in Table 9.

The numerical results of our joint fits are listed in Tables 10 and 11, and the resulting plots are shown in Figures 13, 14, and 15. We found that, using the TIC-derived stellar parameters, TOI-1450A b has a mass of $1.26 \pm 0.13\,M_\oplus$ and a radius of $1.13 \pm 0.04\,R_\oplus$. This corresponds to a density of 4.8 ± 0.7 g cm^{-3}. If we instead use the SED-derived stellar radius and mass, we recover a planet mass of $1.27 \pm 0.13\,M_\oplus$ and a radius of $1.16 \pm 0.07\,R_\oplus$, leading to a density of 4.6 ± 1.0 g cm^{-3}. These values are all within 1σ of the planet parameters using the TIC-derived stellar parameters. This demonstrates that our measured planet mass is somewhat robust to changes in how the stellar parameters are calculated. For the purposes of this paper, we will use the planet parameters derived using the TIC stellar parameters given their higher precision and empirically calculated nature.

Our extensive data set allows us to measure the mass of the transiting planet with a 10% precision despite its very small size and the complicating influence of the additional planet, activity signal, and near-integer-day orbital period. We are confident in our precise mass measurement, as we found that our derived planet mass was insensitive to our model choice or method for determining stellar mass.

6. Discussion

6.1. Dynamics

We must check to see if the reported planet system is stable before claiming a detection, especially given the fact that there is some ambiguity in the model selection. An analysis which shows that the system is dynamically stable on long timescales would support the two-planet model selected in Section 5.2.1. We can do so quickly with an analytical method inspired by Lissauer et al. (2011), which makes use of the mutual Hill sphere radius:

$$R_{H_{i,o}} = \left(\frac{M_i + M_o}{3M_\star}\right)^{1/3} \frac{a_i + a_o}{2}, \quad (2)$$

where i and o are adjacent planet indices, with i being an inner planet and o being an outer planet. The dynamical orbital

Table 9
The Priors Used in the RV Fit

Fit Parameters	
P_b (days)	N(2.04392, 0.0001)
P_c (days)	U(4, 5.5)
$t_{0,b}$ (BJD)	N(2458685.3434, 0.005)
$t_{0,c}$ (BJD)	U(2459321, 2459326.5)
K_b (m s^{-1})	U(0, 3)
K_c (m s^{-1})	U(0, 3)
e_{bc}	0 (fixed)
ω_{bc}	90 (fixed)
$\rho_\star$ (g cm^{-3})	N(6.4, 1)
$\mu_{\rm Apr21,R}$ (m s^{-1})	U(−10, 10)
$\mu_{\rm Apr21,B}$ (m s^{-1})	U(−10, 10)
$\mu_{\rm May21,R} - \mu_{\rm Apr21,R}$ (m s^{-1})	N(2.5, 1)
$\mu_{\rm May21,B} - \mu_{\rm Apr21,B}$ (m s^{-1})	N(2.5, 1)
$\mu_{\rm Aug21,R}$ (m s^{-1})	U(−10, 10)
$\mu_{\rm Aug21,B}$ (m s^{-1})	U(−10, 10)
$\mu_{\rm Nov21,R} - \mu_{\rm Aug21,R}$ (m s^{-1})	N(2.5, 1)
$\mu_{\rm Nov21,B} - \mu_{\rm Aug21,B}$ (m s^{-1})	N(1.5, 1)
$\mu_{\rm Mar22,R}$ (m s^{-1})	U(−10, 10)
$\mu_{\rm Mar22,B}$ (m s^{-1})	U(−10, 10)
$\mu_{\rm May22,R} - \mu_{\rm Mar22,R}$ (m s^{-1})	N(1.5, 1)
$\mu_{\rm May22,B} - \mu_{\rm Mar22,B}$ (m s^{-1})	N(−1.5, 1)
$\mu_{\rm Jul/Aug22,R} - \mu_{\rm Mar22,R}$ (m s^{-1})	N(3.7, 1.12)
$\mu_{\rm Jul/Aug22,B} - \mu_{\rm Mar22,B}$ (m s^{-1})	N(0.5, 1.41)
$\mu_{\rm Jul23,R}$ (m s^{-1})	U(−10, 10)
$\mu_{\rm Jul23,B}$ (m s^{-1})	U(−10, 10)
$\ln\sigma_{\rm all}$ (m s^{-1})	U(ln(0.001), ln(5))
$\ln\sigma_{\rm GP,red}$	U(ln(0.01), ln(4))
$\ln\sigma_{\rm GP,blue}$	U(ln(0.01), ln(4))
$\ln\alpha_{\rm GP}$	U(ln(1.5 × 10^{-6}), ln(6.25 × 10^{-4}))
$\ln\Gamma_{\rm GP}$	U(ln(0.01), ln(10))
$P_{\rm rot}$	N(40, 3)

Notes. The joint-fit model included both these priors and the transit priors from Table 5. The lnσ for the different MAROON-X runs and channels are being fit separately, but all share the same priors so we omit listing them individually in this table.

Table 10
The Planet Parameters from the `juliet` Fit to Both the Detrended TESS Data and the MAROON-X RV Data

Fit Parameters	b	c
P (days)	2.0439274 ± 0.0000010	5.0688 ± 0.0019
t_0 (BJD)	2458685.34221 ± 0.00042	2459321.76 ± 0.16
r_1	0.8243 ± 0.0147	⋯
r_2	0.0219 ± 0.0005	⋯
$\rho_\star$ (g cm^{-3})	6.42 ± 0.63	
K (m s^{-1})	1.05 ± 0.10	0.94 ± 0.11
Derived Parameters		
$a/R_\star$	11.23 ± 0.37	-
R_p ($R_\oplus$)	1.130 ± 0.043	-
b	0.737 ± 0.022	⋯
I (degrees)	86.245 ± 0.237	⋯
$T_{\rm dur}$ (hr)	0.988 ± 0.013	⋯
$T_{\rm eq}$ (K)	722 ± 35	533 ± 26
$M\sin i$ ($M_\oplus$)	1.256 ± 0.128	1.527 ± 0.181
M ($M_\oplus$)	1.258 ± 0.128	⋯

Table 11
The Instrument Parameters from the `juliet` Fit to Both the Detrended TESS Data and the MAROON-X RV Data

Transit Parameters						
Instrument	μ (ppm)	σ (ppm)	q_1	q_2	u_1	u_2
TESS_{120s}	-2 ± 22	15^{+21}_{-10}	$0.30^{+0.24}_{-0.17}$	$0.34^{+0.40}_{-0.24}$	0.33 ± 0.29	0.15 ± 0.32
TESS_{20s}	10 ± 18	863^{+26}_{-26}	$0.32^{+0.17}_{-0.15}$	$0.52^{+0.30}_{-0.30}$	0.54 ± 0.30	-0.03 ± 0.30
$\mathrm{Sinistro}_{\mathrm{Jul}}$	26 ± 105	1140^{+77}_{-95}	$0.46^{+0.35}_{-0.30}$	$0.60^{+0.28}_{-0.36}$	0.69 ± 0.46	-0.09 ± 0.39
$\mathrm{Sinistro}_{\mathrm{Aug}}$	2 ± 81	830^{+73}_{-89}	$0.73^{+0.17}_{-0.29}$	$0.68^{+0.23}_{-0.31}$	1.09 ± 0.45	-0.28 ± 0.40
$\mathrm{MuSCAT3}_g$	-3 ± 61	557^{+79}_{-73}	$0.54^{+0.31}_{-0.34}$	$0.58^{+0.25}_{-0.35}$	0.75 ± 0.45	-0.09 ± 0.38
$\mathrm{MuSCAT3}_r$	30 ± 68	1725^{+51}_{-60}	$0.49^{+0.31}_{-0.27}$	$0.41^{+0.37}_{-0.27}$	0.48 ± 0.42	0.10 ± 0.39
$\mathrm{MuSCAT3}_i$	24 ± 74	2243^{+61}_{-62}	$0.40^{+0.38}_{-0.27}$	$0.52^{+0.32}_{-0.36}$	0.55 ± 0.42	-0.02 ± 0.38
$\mathrm{MuSCAT3}_z$	27 ± 58	2098^{+47}_{-42}	$0.40^{+0.34}_{-0.27}$	$0.43^{+0.36}_{-0.29}$	0.46 ± 0.41	0.07 ± 0.37

RV Parameters		
Parameter	Red	Blue
μ_{Apr21} (m s^{-1})	-7.12 ± 0.80	-7.36 ± 0.99
$\mu_{\mathrm{May21}} - \mu_{\mathrm{Apr21,R}}$ (m s^{-1})	2.81 ± 0.75	2.71 ± 0.87
μ_{Aug21} (m s^{-1})	-4.99 ± 0.79	-2.81 ± 1.08
$\mu_{\mathrm{Nov21}} - \mu_{\mathrm{Aug21,R}}$ (m s^{-1})	2.44 ± 0.77	1.52 ± 0.84
μ_{Mar22} (m s^{-1})	1.45 ± 0.57	1.17 ± 0.71
$\mu_{\mathrm{May22}} - \mu_{\mathrm{Mar22,R}}$ (m s^{-1})	1.64 ± 0.77	-0.87 ± 0.92
$\mu_{\mathrm{Jul/Aug22}-\mu_{\mathrm{Mar22,R}}}$ (m s^{-1})	3.31 ± 0.69	0.67 ± 0.87
μ_{Jul23} (m s^{-1})	6.84 ± 0.79	4.70 ± 1.06
σ_{Apr21} (m s^{-1})	$0.79^{+0.80}_{-0.72}$	$0.03^{+0.34}_{-0.02}$
σ_{May21} (m s^{-1})	$0.46^{+0.13}_{-0.22}$	$0.51^{+0.45}_{-0.50}$
σ_{Aug21} (m s^{-1})	$0.03^{+0.31}_{-0.03}$	$0.20^{+1.13}_{-0.19}$
σ_{Nov21} (m s^{-1})	$0.02^{+0.17}_{-0.02}$	$0.04^{+0.26}_{-0.04}$
σ_{Mar22} (m s^{-1})	$0.70^{+0.39}_{-0.64}$	$0.05^{+0.30}_{-0.05}$
σ_{May22} (m s^{-1})	$0.03^{+0.26}_{-0.03}$	$0.37^{+1.13}_{-0.36}$
$\sigma_{\mathrm{Jul/Aug22}}$ (m s^{-1})	$0.01^{+0.18}_{-0.01}$	$0.06^{+0.49}_{-0.05}$
σ_{Jul23} (m s^{-1})	$0.05^{+0.22}_{-0.05}$	$0.02^{+0.12}_{-0.01}$

GP Parameters	
$\sigma_{\mathrm{GP,red}}$	1.40 ± 0.22
$\sigma_{\mathrm{GP,blue}}$	1.85 ± 0.30
α_{GP}	$0.000025^{+0.000196}_{-0.000022}$
Γ_{GP}	$8.70^{+0.89}_{1.40}$
P_{rot}	$40.1^{+1.7}_{-1.5}$

separation Δ is defined as

$$\Delta = \frac{a_o - a_i}{R_{H_{i,o}}}. \quad (3)$$

If we assume that the planets are roughly coplanar and that $\sin i \approx 1$, Δ_{cb} is approximately equal to 33. As shown in Gladman (1993), a pair of small planets on circular orbits with $\Delta > 2\sqrt{3}$ are stable against close approaches for very long periods of time. This indicates that this system would be stable if there are no other planets in the system.

If a planet is present at 3.18 days or 3.39 days (and thus in three-body resonance with the other two planets) $\Delta > 9$ even if the 3 days planet had a mass of $\geqslant 10\,M_{\oplus}$. If such a planet were present, it would also satisfy the stability boundary for three-planet systems discussed in Lissauer et al. (2011), which would be fulfilled if

$$\Delta_{cb} + \Delta_{dc} > 18. \quad (4)$$

If this planet were present, the planets would be relatively evenly spaced, aligning with the "peas-in-a-pod" pattern of orbital spacing noted in the Kepler transiting planet sample by Weiss et al. (2018). With period ratios 1.5–1.7, the system would fall on the boundary between correlated and uncorrelated period ratios described in Jiang et al. (2020), which concluded that evenly spaced period ratios are likely the result of mean motion resonances. If the TOI-1450A planetary system is the result of disk-driven inward planet migration, we may expect to see the presence of this additional planet.

Regarding the secondary star, we note that Ballantyne et al. (2021) states that, if the binary stars TOI-1450A and TOI-1450B have a circular orbit, any planet orbiting the primary with $a \leqslant 28.6$ au is stable with respect to the binary system. As all of the planets discussed here have a measured a well within this limit, it is clear that this system should be stable with regards to the companion star.

6.2. Transiting Planet Composition

With our joint fit, we find that the transiting planet has a mass of $M_p = 1.26 \pm 0.13\,M_{\oplus}$ and a radius of $R_p = 1.13 \pm$

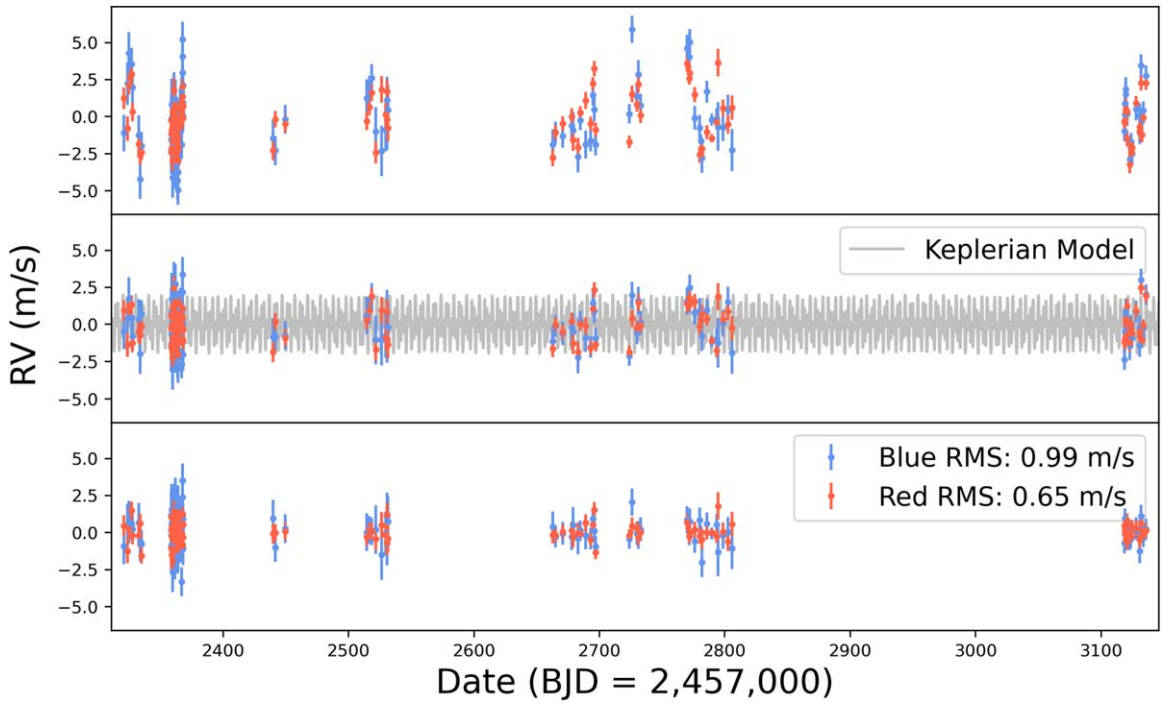

Figure 13. Top: the offset-subtracted RV data for TOI-1450A. The MAROON-X red and blue channels are colored accordingly. Middle: the RV data with both the offsets and best-fit GPs subtracted. The best-fitting two-planet Keplerian model is shown in gray. Bottom: the data residuals (subtracting out the offsets, GPs, and best-fit Keplerians).

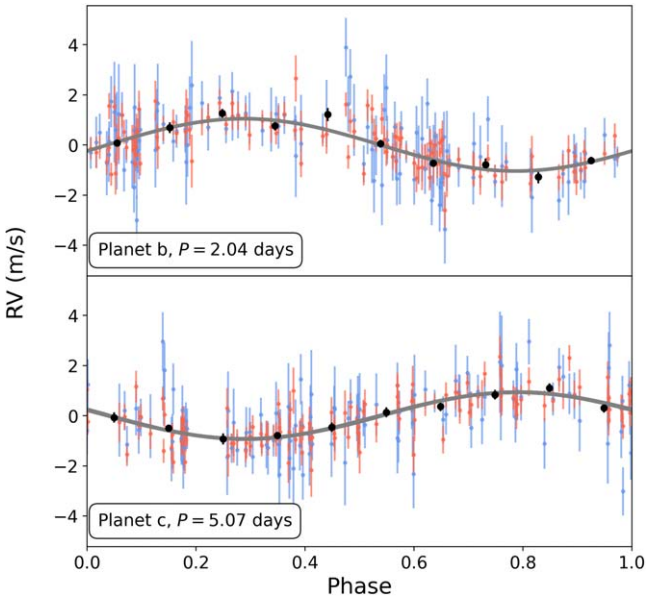

Figure 14. The phase-folded RVs for TOI-1450A b and TOI-1450A c. The offsets, activity, and other planets are subtracted out in each panel to focus on the relevant signal. The MAROON-X red and blue channels are colored accordingly, and binned data are shown in black. The best-fit model is shown in gray.

$0.04\,R_{\oplus}$. Given our knowledge of the mass and radius of the planet, we can estimate its internal composition using the `ManipulatePlanet` tool (Zeng & Sasselov 2013; Zeng et al. 2016). `ManipulatePlanet` solves for the planet's structure based on an extrapolation based on Earth's seismic density profile. It estimates the planet's iron, water, and rock contents, though these values are somewhat degenerate with the planet's central pressure, which is an unknown value. We note that this code assumes an atmosphere is not present, which means that it may underestimate the iron content of the planet.

The resulting ternary diagram from `ManipulatePlanet` is shown in Figure 16. It appears that this planet may have a core mass fraction that is lower than that of the Earth ($32.5\% \pm 0.3\%$; Wang et al. 2018), though mass and radius measurements are not precise enough to allow for a better composition estimate. More precision as to the mass and radius measurements will be necessary to prove whether or not this planet is less dense than the Earth. TOI-1450A b's low density could hint at the presence of an atmosphere, but could also just be a sign of a small core or an enhanced bulk volatile composition, which is possible if the planet formed at larger orbital separations and migrated inward (see, e.g., the results of the simulations from Burn et al. 2021). Even if it does possess an atmosphere, however, its high equilibrium temperature rules out the possibility of the planet being habitable, even when adopting the most optimistic HZ limits from Kopparapu et al. (2016).

Figure 17 shows where TOI-1450A b sits on a mass–radius plot compared to other exoplanets downloaded from TEPCat (Southworth 2011) as of 2024 May 2. Composition models from Zeng et al. (2019) are overplotted for comparison. TOI-1450A b appears to have a lower density than what we would expect from an Earth-like planet, indicating that it either lacks a core or has some meaningful volatile component. If we adopt the stellar parameters from SED fitting, the planet has an even lower density. However, a higher mass precision (and better stellar parameter characterization) will be necessary to make any confident conclusions about the planet's composition. We also note that TOI-1450A b is one of the lowest-mass planets with a sub-20% mass error, with the only smaller (and more precise) planet masses being the TTV-derived masses of the

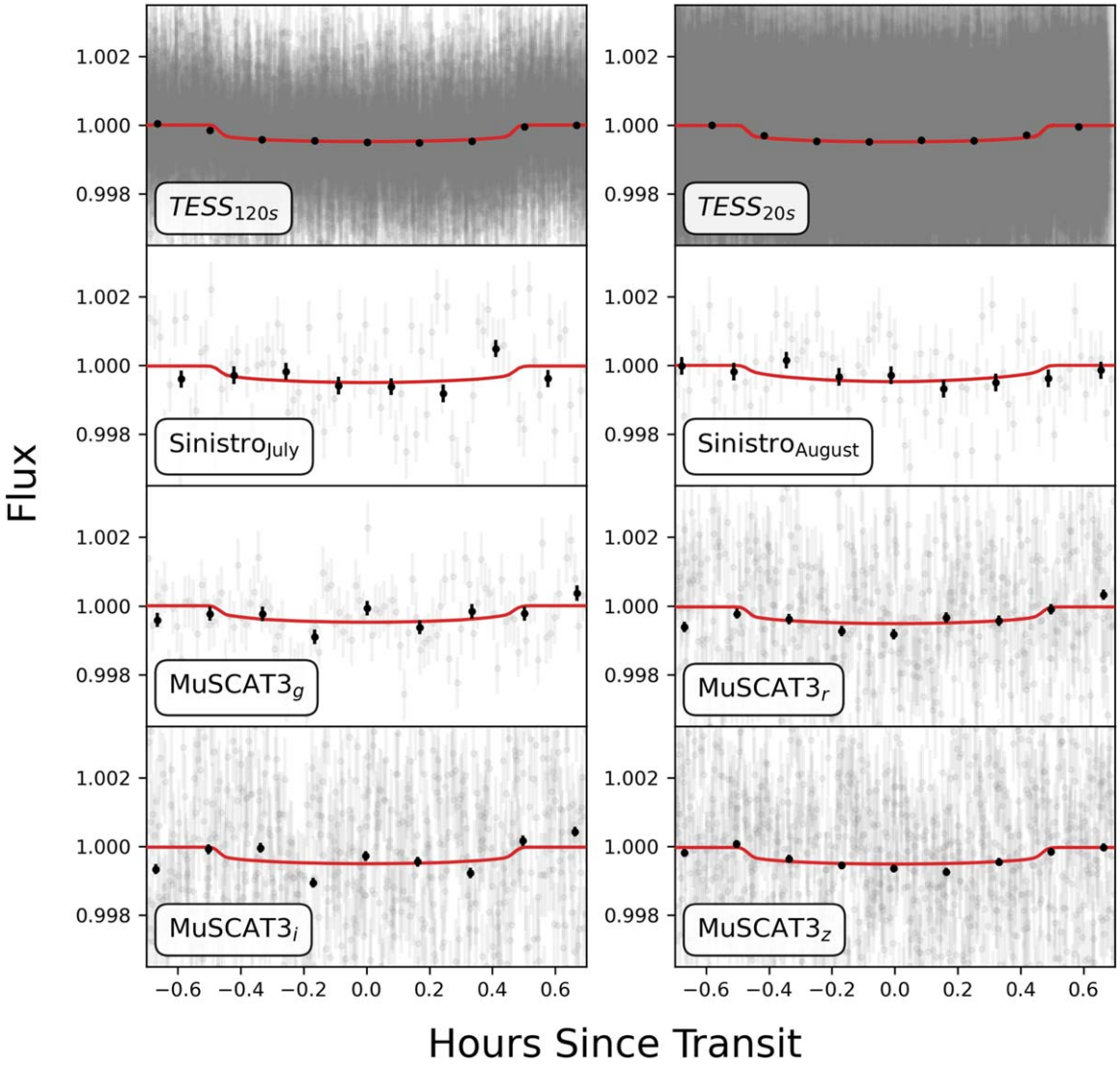

Figure 15. The phase-folded transit data for TOI-1450A b, with our best-fit model shown in red. Binned data are shown as black points. Each panel highlights a different data set.

TRAPPIST-1 system and the RV-derived mass of the ultra-short-period planet GJ 367 b (Goffo et al. 2023). TOI-1450A b is the second-lowest-mass planet with a precise RV mass.

We can only estimate the minimum mass of TOI-1450A c. If it is coplanar with TOI-1450A b, with $i \approx 86°$, it has a mass of about 1.5 $M_{\oplus}$, making it only slightly larger than the Earth. It could be very similar in composition to TOI-1450A b, though it is impossible to estimate its composition without a radius measurement.

6.3. Suitability for Atmospheric Characterization

Our measured mass precision for TOI-1450A b is approximately 10%. As the measured error is less than 20%, the planet's mass precision is now at the level that the planet is amenable to high-precision atmospheric characterization with JWST (Batalha et al. 2019). However, it is first important to determine whether or not the planet is suitable for such a measurement. Kempton et al. (2018) created two metrics for the purpose of identifying transiting planets most suitable for atmospheric characterization. These are primarily useful for prioritizing planets for follow-up studies with JWST.

The transmission spectroscopy metric (TSM) gives a description of how suitable the planet is for transmission spectroscopy. Assuming a low albedo, TOI-1450A b has a TSM of 14.3 ± 2.1. This value is slightly (but not significantly) higher if we assume the SED-derived stellar characteristics, with a TSM of 14.5 ± 2.4. Given the planet's small radius, it is above the TSM = 12 threshold described by Kempton et al. (2018) for high-quality atmospheric characterization targets, though only at the $\approx 1\sigma$ level. As TOI-1450A b has a very similar mass and radius to that of the Earth, it at least superficially appears that this target should be prioritized for follow-up atmospheric characterization efforts. However, given its low mass and short orbital period, it is possible that any substantial atmosphere that the planet may have had has already been lost.

We can estimate the photoevaporative mass-loss rate of the planet's atmosphere given the following equation from

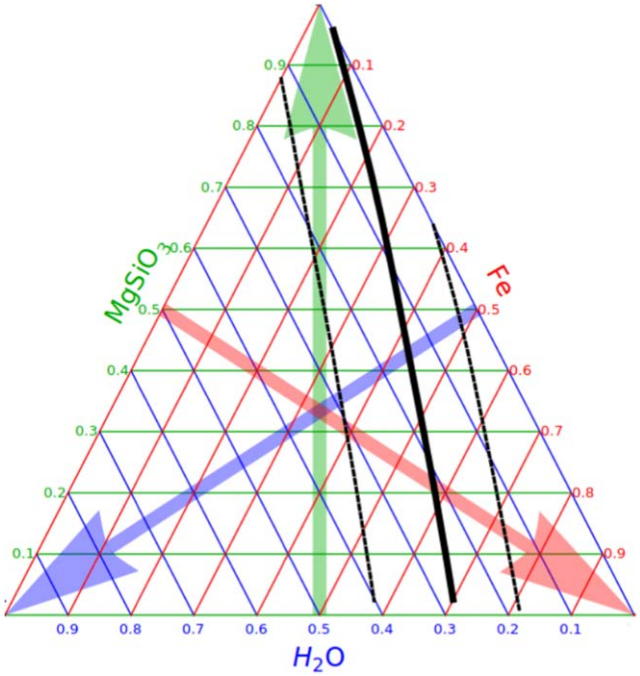

Figure 16. Ternary diagram of the composition of TOI-1450A b generated using `ManipulatePlanet` (Zeng & Sasselov 2013; Zeng et al. 2016). The solid black line indicates the planet composition for a variety of different central pressure values, while the dotted black lines indicate the range of values given the mass and radius errors.

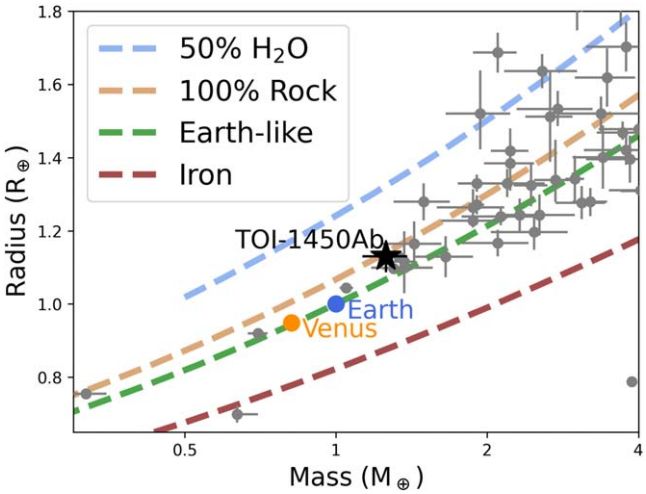

Figure 17. The mass and radius of TOI-1450Ab (black star) compared to both interior composition models from Zeng et al. (2019; colored dashed lines) and other exoplanets with mass and radius errors <20% from TEPCat (gray points). Earth and Venus are also included for reference.

Sanz-Forcada et al. (2011):

$$\dot{M} = \frac{\pi R_p^3 F_{\rm XUV}}{GKM_p}, \quad (5)$$

where $F_{\rm XUV}$ is the X-ray and ultraviolet (XUV) flux of the host star at the planet's orbit, G is the gravitational constant, and K is a term that describes the potential energy reduction due to tidal forces, using the formula from Erkaev et al. (2007).

While there are no direct $F_{\rm XUV}$ measurements of the host star, Freund et al. (2022) identified that a point X-ray source from the Second ROSAT all-sky survey (Boller et al. 2016) seemed to roughly correspond with the known R.A. and decl. of TOI-1450A. However, the X-ray flux of this source (2.56×10^{-14} erg s^{-1} cm^{-2}) is close to the detection limit of the instrument, and the resolution of the instrument is low enough that this source likely also includes the light from TOI-1450B, so we can consider this X-ray flux to be an upper limit. Given the star's distance from Gaia Collaboration (2020), this corresponds to an X-ray luminosity $L_{\rm X}$ of 1.54×10^{27} erg s^{-1}. As there are no available extreme-ultraviolet (EUV) flux measurements of the host star, we used the relation from Sanz-Forcada et al. (2011) to estimate the EUV luminosity, finding $L_{\rm EUV} \approx 1.5 \times 10^{28}$ erg s^{-1}, though we note that this relation has a high degree of scatter. This results in a $F_{\rm XUV}$ at the planet's orbit of about 9.7×10^3 erg s^{-1} cm^{-2}. Plugging these numbers into the above equation, we find that $\dot{M} \approx 0.12$ $M_\oplus$ Gyr^{-1}. This mass-loss rate seems to be high enough that it would indicate that the planet could lose any substantial atmosphere over the course of its life, especially given that the host star likely had a higher XUV flux earlier in its lifetime. However, we note that the X-ray flux is a likely upper limit and the method used to estimate the EUV flux is imprecise, so it is certainly possible that the actual mass-loss rate is much slower. The current data are insufficient to conclude whether or not TOI-1450A b has lost its atmosphere.

We can evaluate the likelihood of TOI-1450A b having an atmosphere by comparing it to similar planets with JWST measurements. TRAPPIST-1 b, which superficially resembles TOI-1450A b in that it is a roughly Earth-sized M-dwarf planet at an orbital period of <3 days (see, e.g., Agol et al. 2021), was recently observed by JWST and found to have little to no atmosphere (Greene et al. 2023). As TOI-1450A b has an even higher equilibrium temperature than TRAPPIST-1 b, it seems possible that it was able to undergo more extreme atmospheric loss. However, TRAPPIST-1 has a much later spectral type than TOI-1450A, which could be influential on the planet's atmosphere due to the star's enhanced activity levels and longer activity lifetime (Hawley et al. 2000). TOI-1450A b is a challenging target with MIRI/LRS as envisioned by Kempton et al. (2018). However, Greene et al. (2023) and Zieba et al. (2023) have been able to successfully detect the thermal emission of TRAPPIST-1 b and TRAPPIST-1 c (which have lower emission spectroscopy metrics) at 15 μm, demonstrating that these challenging targets can still be characterized with JWST at longer wavelengths.

7. Summary and Conclusions

TOI-1450 is a binary star system with a mid-M primary and a late-M secondary component. The two stars are too close to separate on an individual TESS pixel, complicating efforts at follow-up given the secondary's strong rotation signal. However, by performing a follow-up RV survey of TOI-1450 A with MAROON-X, we were able to confirm the presence of a 2.044 days planet signal that transits the primary star at the correct period and phase, and found that it is consistent with a $1.13 \pm 0.04\,R_\oplus$ planet with a mass of $1.26 \pm 0.13\,M_\oplus$. This planet has a density consistent with Earth (given the models from Zeng et al. 2019), but could also possess some volatiles or even an atmospheric envelope given its slightly sub-Earth density. Given its mass and radius, TOI-1450A b is above the cutoff for suitability for atmospheric transmission spectrum characterization with JWST, which may provide us with an interesting opportunity to study the atmosphere of a hot, low-density M-dwarf planet. However,

given the planet's short orbital period, it is unclear whether or not TOI-1450A b would be able to retain an atmosphere over long periods of time, necessitating further modeling efforts. We also discovered the presence of an additional nontransiting planet in the system with a 5.07 days period and a $M_p \sin i_p$ similar to TOI-1450A b.

In addition, while the photometric data contains a sinusoidal 2 days signal that is likely a rotation signal, we were able to use a combination of spectroscopic activity indicators and chromatic RV signals to support the hypothesis that TOI-1450B is the rapid rotator in the system. Additionally, spectroscopic activity indicators and undetrended TESS photometry support a roughly 40 days rotation period for TOI-1450A—a long enough rotation period that the star's rotation is unlikely to strongly influence our results.

Acknowledgments

This material is based upon work supported by the National Science Foundation Graduate Research Fellowship under grant No. DGE 1746045. G.S. acknowledges support provided by NASA through the NASA Hubble Fellowship grant No. HST-HF2-51519.001-A awarded by the Space Telescope Science Institute, which is operated by the Association of Universities for Research in Astronomy, Inc., for NASA, under contract NAS5-26555. This work is partly supported by JSPS KAKENHI grant No. JP18H05439 and JST CREST grant No. JPMJCR1761. This research has also made use of NASA's Astrophysics Data System Bibliographic Services.

The University of Chicago group acknowledges funding for the MAROON-X project from the David and Lucile Packard Foundation, the Heising-Simons Foundation, the Gordon and Betty Moore Foundation, the Gemini Observatory, the NSF (award number 2108465), and NASA (grant No. 80NSSC 22K0117). The Gemini observations are associated with programs GN-21A-Q-120, GN-21B-Q-216, GN-22A-Q-120, GN-22A-Q-218, GN-22B-Q-214, and GN-23A-Q-120 (PI: Bean).

Resources supporting this work were provided by the NASA High-End Computing Capability (HECC) Program through the NASA Advanced Supercomputing (NAS) Division at Ames Research Center for the production of the SPOC data products.

This work makes use of observations from the LCOGT network. Part of the LCOGT telescope time was granted by NOIRLab through the Mid-Scale Innovations Program (MSIP). MSIP is funded by NSF.

This research has made use of the Exoplanet Follow-up Observation Program (ExoFOP; doi:10.26134/ExoFOP5) website, which is operated by the California Institute of Technology, under contract with the National Aeronautics and Space Administration under the Exoplanet Exploration Program.

Funding for the TESS mission is provided by NASA's Science Mission Directorate. K.A.C. and C.N.W. acknowledge support from the TESS mission via subaward s3449 from MIT. We acknowledge the use of public TESS data from pipelines at the TESS Science Office and at the TESS Science Processing Operations Center.

This paper is based on observations made with the MuSCAT3 instrument, developed by the Astrobiology Center and under financial supports by JSPS KAKENHI (grant No. JP18H05439) and JST PRESTO (grant No. JPMJPR1775), at Faulkes Telescope North on Maui, HI, operated by the Las Cumbres Observatory.

Some of the data presented in this paper were obtained from the Mikulski Archive for Space Telescopes (MAST) at the Space Telescope Science Institute. The specific observations analyzed can be accessed via MAST Team (2021).

Facilities: Exoplanet Archive, LCOGT.

Software: AstroImageJ (Collins et al. 2017), Astropy (Astropy Collaboration et al. 2013, 2018, 2022), astroquery (Ginsburg et al. 2019), batman (Kreidberg 2015), dynesty (Speagle 2020), emcee (Foreman-Mackey et al. 2013), exoplanet (Foreman-Mackey et al. 2020), juliet (Espinoza et al. 2019), lightkurve (Lightkurve Collaboration et al. 2018), Numpy (Harris et al. 2020), PyAstronomy (Czesla et al. 2019), PyMC3 (Salvatier et al. 2016), Scipy (Virtanen et al. 2020), spectres (Carnall 2017), TAPIR (Jensen 2013), theano (Theano Development Team 2016), tpfplotter (Aller et al. 2020).

ORCID iDs

Madison Brady https://orcid.org/0000-0003-2404-2427
Jacob L. Bean https://orcid.org/0000-0003-4733-6532
Andreas Seifahrt https://orcid.org/0000-0003-4526-3747
David Kasper https://orcid.org/0000-0003-0534-6388
Rafael Luque https://orcid.org/0000-0002-4671-2957
Guðmundur Stefánsson https://orcid.org/0000-0001-7409-5688
Julian Stürmer https://orcid.org/0000-0002-4410-4712
David Charbonneau https://orcid.org/0000-0002-9003-484X
Karen A. Collins https://orcid.org/0000-0001-6588-9574
John P. Doty https://orcid.org/0000-0003-2996-8421
Zahra Essack https://orcid.org/0000-0002-2482-0180
Akihiko Fukui https://orcid.org/0000-0002-4909-5763
Ferran Grau Horta https://orcid.org/0000-0001-9927-7269
Christina Hedges https://orcid.org/0000-0002-3385-8391
Coel Hellier https://orcid.org/0000-0002-3439-1439
Jon M. Jenkins https://orcid.org/0000-0002-4715-9460
Norio Narita https://orcid.org/0000-0001-8511-2981
Samuel N. Quinn https://orcid.org/0000-0002-8964-8377
Avi Shporer https://orcid.org/0000-0002-1836-3120
Richard P. Schwarz https://orcid.org/0000-0001-8227-1020
Sara Seager https://orcid.org/0000-0002-6892-6948
Keivan G. Stassun https://orcid.org/0000-0002-3481-9052
Stephanie Striegel https://orcid.org/0009-0008-5145-0446
Cristilyn N. Watkins https://orcid.org/0000-0001-8621-6731
Joshua N. Winn https://orcid.org/0000-0002-4265-047X

References

Agol, E., Dorn, C., Grimm, S. L., et al. 2021, PSJ, 2, 1
Aigrain, S., Pont, F., & Zucker, S. 2012, MNRAS, 419, 3147
Aller, A., Lillo-Box, J., Jones, D., Miranda, L. F., & Barceló Forteza, S. 2020, A&A, 635, A128
Astropy Collaboration, Price-Whelan, A. M., Lim, P. L., et al. 2022, ApJ, 935, 167
Astropy Collaboration, Price-Whelan, A. M., Sipőcz, B. M., et al. 2018, AJ, 156, 123
Astropy Collaboration, Robitaille, T. P., Tollerud, E. J., et al. 2013, A&A, 558, A33
Ballantyne, H. A., Espaas, T., Norgrove, B. Z., et al. 2021, MNRAS, 507, 4507
Baraffe, I., Homeier, D., Allard, F., & Chabrier, G. 2015, A&A, 577, A42
Barnes, R. 2017, CeMDA, 129, 509
Batalha, N. E., Lewis, T., Fortney, J. J., et al. 2019, ApJL, 885, L25
Bean, J. L., Seifahrt, A., Hartman, H., et al. 2010, ApJ, 713, 410
Boller, T., Freyberg, M. J., Trümper, J., et al. 2016, A&A, 588, A103
Borucki, W. J., Koch, D., Basri, G., et al. 2010, Sci, 327, 977

Boyajian, T. S., von Braun, K., van Belle, G., et al. 2012, ApJ, 757, 112
Brady, M., Bean, J. L., Seifahrt, A., et al. 2023, AJ, 165, 129
Brady, M. T., & Bean, J. L. 2022, AJ, 163, 255
Brown, T. M., Baliber, N., Bianco, F. B., et al. 2013, PASP, 125, 1031
Burn, R., Schlecker, M., Mordasini, C., et al. 2021, A&A, 656, A72
Caballero, J. A., Gonzalez-Alvarez, E., Brady, M., et al. 2022, A&A, 665, A120
Canto Martins, B. L., Gomes, R. L., Messias, Y. S., et al. 2020, ApJS, 250, 20
Carnall, A. C. 2017, arXiv:1705.05165
Collins, K. 2019, AAS Meeting Abstracts, 233, 140.05
Collins, K. A., Kielkopf, J. F., Stassun, K. G., & Hessman, F. V. 2017, AJ, 153, 77
Cutri, R. M., Skrutskie, M. F., van Dyk, S., et al. 2003, VizieR On-line Data Catalog, II/246
Czesla, S., Schröter, S., Schneider, C. P., et al., 2019 PyA: Python Astronomy-related Packages, Astrophysics Source Code Library, ascl:1906.010
Davenport, J. R. A., Covey, K. R., Clarke, R. W., et al. 2019, ApJ, 871, 241
Dungee, R., van Saders, J., Gaidos, E., et al. 2022, ApJ, 938, 118
Engle, S. G., & Guinan, E. F. 2023, ApJL, 954, L50
Erkaev, N. V., Kulikov, Y. N., Lammer, H., et al. 2007, A&A, 472, 329
Espinoza, N. 2018, RNAAS, 2, 209
Espinoza, N., Kossakowski, D., & Brahm, R. 2019, MNRAS, 490, 2262
Fauchez, T. J., Villanueva, G. L., Schwieterman, E. W., et al. 2020, NatAs, 4, 372
Foreman-Mackey, D., Agol, E., Angus, R., & Ambikasaran, S. 2017, AJ, 154, 220
Foreman-Mackey, D., Hogg, D. W., Lang, D., & Goodman, J. 2013, PASP, 125, 306
Foreman-Mackey, D., Luger, R., Czekala, I., et al., 2020 exoplanet-dev/exoplanet, v0.4.0, Zenodo, doi:10.5281/zenodo.1998447
Freund, S., Czesla, S., Robrade, J., Schneider, P. C., & Schmitt, J. H. M. M. 2022, A&A, 664, A105
Fulton, B. J., Petigura, E. A., Howard, A. W., et al. 2017, AJ, 154, 109
Gaia Collaboration 2020, yCat, I/350
Ginsburg, A., Sipőcz, B. M., Brasseur, C. E., et al. 2019, AJ, 157, 98
Giovinazzi, M. R., & Blake, C. H. 2022, AJ, 164, 164
Gladman, B. 1993, Icar, 106, 247
Goffo, E., Gandolfi, D., Egger, J. A., et al. 2023, ApJL, 955, L3
Gray, D. F. 2005, The Observation and Analysis of Stellar Photospheres (Cambridge: Cambridge Univ. Press)
Gray, D. F. 2008, The Observation and Analysis of Stellar Photospheres (Cambridge: Cambridge Univ. Press)
Greene, T. P., Bell, T. J., Ducrot, E., et al. 2023, Nature, 618, 39
Guerrero, N. M., Seager, S., Huang, C. X., et al. 2021, ApJS, 254, 39
Hara, N. C., Bouchy, F., Stalport, M., et al. 2020, A&A, 636, L6
Hara, N. C., Boué, G., Laskar, J., & Correia, A. C. M. 2017, MNRAS, 464, 1220
Harris, C. R., Millman, K. J., van der Walt, S. J., et al. 2020, Natur, 585, 357
Hawley, S., Reid, I. N., & Gizis, J. 2000, in ASP Conf. Ser. 212, From Giant Planets to Cool Stars, ed. C. A. Griffith & M. S. Marley (San Francisco, CA: ASP), 252
Hawley, S. L., Gizis, J. E., & Reid, I. N. 1996, AJ, 112, 2799
Hippke, M., & Heller, R. 2019, A&A, 623, A39
Huang, C. X., Vanderburg, A., Pál, A., et al. 2020a, RNAAS, 4, 204
Huang, C. X., Vanderburg, A., Pál, A., et al. 2020b, RNAAS, 4, 206
Husser, T. O., Wende-von Berg, S., Dreizler, S., et al. 2013, A&A, 553, A6
Jenkins, J. M. 2002, ApJ, 575, 493
Jenkins, J. M., Chandrasekaran, H., McCauliff, S. D., et al. 2010, Proc. SPIE, 7740, 77400D
Jenkins, J. M., Tenenbaum, P., Seader, S., et al. 2020, Kepler Science Document KSCI-19081-002, 9
Jenkins, J. M., Twicken, J. D., McCauliff, S., et al. 2016, Proc. SPIE, 9913, 99133E
Jensen, E., 2013 Tapir: A Web Interface for Transit/eclipse Observability, Astrophysics Source Code Library, ascl:1306.007
Jiang, C.-F., Xie, J.-W., & Zhou, J.-L. 2020, AJ, 160, 180
Kausch, W., Noll, S., Smette, A., et al. 2015, A&A, 576, A78
Kempton, E. M. R., Bean, J. L., Louie, D. R., et al. 2018, PASP, 130, 114401
Kipping, D. M. 2013, MNRAS, 435, 2152
Kochanek, C. S., Shappee, B. J., Stanek, K. Z., et al. 2017, PASP, 129, 104502
Kopparapu, R. k., Wolf, E. T., Haqq-Misra, J., et al. 2016, ApJ, 819, 84
Kreidberg, L. 2015, PASP, 127, 1161
Lépine, S., Hilton, E. J., Mann, A. W., et al. 2013, AJ, 145, 102
Li, J., Tenenbaum, P., Twicken, J. D., et al. 2019, PASP, 131, 024506
Lightkurve Collaboration, Cardoso, J. V. D. M., Hedges, C., et al., 2018 Lightkurve: Kepler and TESS Time Series Analysis in Python, Astrophysics Source Code Library, ascl:1812.013
Lissauer, J. J., Ragozzine, D., Fabrycky, D. C., et al. 2011, ApJS, 197, 8
Luger, R., & Barnes, R. 2015, AsBio, 15, 119
Luque, R., & Pallé, E. 2022, Sci, 377, 1211
Mann, A. W., Dupuy, T., Kraus, A. L., et al. 2019, ApJ, 871, 63
Mann, A. W., Feiden, G. A., Gaidos, E., Boyajian, T., & von Braun, K. 2015, ApJ, 804, 64
Marboeuf, U., Thiabaud, A., Alibert, Y., Cabral, N., & Benz, W. 2014, A&A, 570, A36
MAST Team 2021, TESS Light Curves—All Sectors, STScI/MAST, doi:10.17909/t9-nmc8-f686
McCully, C., Volgenau, N. H., Harbeck, D.-R., et al. 2018, Proc. SPIE, 10707, 107070K
Mugrauer, M., & Michel, K.-U. 2020, AN, 341, 996
Muirhead, P. S., Dressing, C. D., Mann, A. W., et al. 2018, AJ, 155, 180
Mulders, G. D., Ciesla, F. J., Min, M., & Pascucci, I. 2015, ApJ, 807, 9
Narita, N., Fukui, A., Yamamuro, T., et al. 2020, Proc. SPIE, 11447, 114475K
Parsons, S. G., Gänsicke, B. T., Marsh, T. R., et al. 2018, MNRAS, 481, 1083
Pass, E. K., Charbonneau, D., Irwin, J. M., & Winters, J. G. 2022, ApJ, 936, 109
Passegger, V. M., Bello-García, A., Ordieres-Meré, J., et al. 2022, A&A, 658, A194
Passegger, V. M., Reiners, A., Jeffers, S. V., et al. 2018, A&A, 615, A6
Pecaut, M. J., & Mamajek, E. E. 2013, ApJS, 208, 9
Pollacco, D. L., Skillen, I., Collier Cameron, A., et al. 2006, PASP, 118, 1407
Popinchalk, M., Faherty, J. K., Kiman, R., et al. 2021, ApJ, 916, 77
Rabus, M., Lachaume, R., Jordán, A., et al. 2019, MNRAS, 484, 2674
Ricker, G. R., Winn, J. N., Vanderspek, R., et al. 2015, JATIS, 1, 014003
Robertson, P., Stefansson, G., Mahadevan, S., et al. 2020, ApJ, 897, 125
Rogers, J. G., Schlichting, H. E., & Owen, J. E. 2023, ApJL, 947, L19
Salvatier, J., Wiecki, T. V., & Fonnesbeck, C. 2016, PeerJ Comp. Sci., 2, e55
Sanz-Forcada, J., Micela, G., Ribas, I., et al. 2011, A&A, 532, A6
Seifahrt, A., Bean, J. L., Kasper, D., et al. 2022, Proc. SPIE, 12184, 121841G
Seifahrt, A., Stürmer, J., Bean, J. L., & Schwab, C. 2018, Proc. SPIE, 10702, 107026D
Shappee, B. J., Prieto, J. L., Grupe, D., et al. 2014, ApJ, 788, 48
Skrutskie, M. F., Cutri, R. M., Stiening, R., et al. 2006, AJ, 131, 1163
Smette, A., Sana, H., Noll, S., et al. 2015, A&A, 576, A77
Smith, J. C., Stumpe, M. C., Van Cleve, J. E., et al. 2012, PASP, 124, 1000
Southworth, J. 2011, MNRAS, 417, 2166
Speagle, J. S. 2020, MNRAS, 493, 3132
Stassun, K. G., Collins, K. A., & Gaudi, B. S. 2017, AJ, 153, 136
Stassun, K. G., Corsaro, E., Pepper, J. A., & Gaudi, B. S. 2018, AJ, 155, 22
Stassun, K. G., Oelkers, R. J., Paegert, M., et al. 2019, AJ, 158, 138
Stassun, K. G., & Torres, G. 2016, AJ, 152, 180
Stassun, K. G., & Torres, G. 2021, ApJL, 907, L33
Stock, S., Kemmer, J., Kossakowski, D., et al. 2023, A&A, 674, A108
STScI 2018, TESS Input Catalog and Candidate Target List, STScI/MAST, doi:10.17909/fwdt-2x66
Stumpe, M. C., Smith, J. C., Catanzarite, J. H., et al. 2014, PASP, 126, 100
Stumpe, M. C., Smith, J. C., Van Cleve, J. E., et al. 2012, PASP, 124, 985
Suárez Mascareño, A., Rebolo, R., González Hernández, J. I., & Esposito, M. 2015, MNRAS, 452, 2745
Sullivan, P. W., Winn, J. N., Berta-Thompson, Z. K., et al. 2015, ApJ, 809, 77
Terrien, R. C., Keen, A., Oda, K., et al. 2022, ApJL, 927, L11
Theano Development Team 2016, arXiv:1605.02688
Thiabaud, A., Marboeuf, U., Alibert, Y., et al. 2014, A&A, 562, A27
Tilley, M. A., Segura, A., Meadows, V., Hawley, S., & Davenport, J. 2019, AsBio, 19, 64
Trotta, R. 2008, ConPh, 49, 71
Twicken, J. D., Catanzarite, J. H., Clarke, B. D., et al. 2018, PASP, 130, 064502
Van Eylen, V., & Albrecht, S. 2015, ApJ, 808, 126
Virtanen, P., Gommers, R., Oliphant, T. E., et al. 2020, NatMe, 17, 261
Wang, H. S., Lineweaver, C. H., & Ireland, T. R. 2018, Icar, 299, 460
Weiss, L. M., Marcy, G. W., Petigura, E. A., et al. 2018, AJ, 155, 48
Wunderlich, F., Godolt, M., Grenfell, J. L., et al. 2019, A&A, 624, A49
Zechmeister, M., & Kürster, M. 2009, A&A, 496, 577
Zechmeister, M., Reiners, A., Amado, P. J., et al., 2020 SERVAL: SpEctrum Radial Velocity AnaLyser, Astrophysics Source Code Library, ascl:2006.011
Zeng, L., Jacobsen, S. B., Sasselov, D. D., et al. 2019, PNAS, 116, 9723
Zeng, L., & Sasselov, D. 2013, PASP, 125, 227
Zeng, L., Sasselov, D. D., & Jacobsen, S. B. 2016, ApJ, 819, 127
Zieba, S., Kreidberg, L., Ducrot, E., et al. 2023, Natur, 620, 746